AGU ADVANCING EARTH AND SPACE SCIENCE

JGR Atmospheres

RESEARCH ARTICLE
10.1029/2019JD031686

Key Points:
- A mixed forest was observed as a larger CO_2 sink/source than a rice paddy due to a longer growing period and stronger ecosystem respiration
- The biogenic sink offsets about 70% of anthropogenic contribution to column-averaged CO_2 concentrations over Northeast China
- Uncertainty of simulated CO_2 fluxes with the WRF-VPRM largely depends on VPRM parameters, in particular maximum light use efficiency

Supporting Information:
- Supporting Information S1

Correspondence to:
X.-M. Hu,
xhu@ou.edu

Citation:
Li, X., Hu, X.-M., Cai, C., Jia, Q., Zhang, Y., Liu, J., et al. (2020). Terrestrial CO_2 fluxes, concentrations, sources and budget in Northeast China: Observational and modeling studies. *Journal of Geophysical Research: Atmospheres*, *125*, e2019JD031686. https://doi.org/10.1029/2019JD031686

Received 17 SEP 2019
Accepted 24 FEB 2020
Accepted article online 3 MAR 2020

Terrestrial CO_2 Fluxes, Concentrations, Sources and Budget in Northeast China: Observational and Modeling Studies

Xiaolan Li[1], Xiao-Ming Hu[2], Changjie Cai[3], Qingyu Jia[1], Yao Zhang[4], Jingmiao Liu[5], Ming Xue[2], Jianming Xu[6], Rihong Wen[1], and Sean M. R. Crowell[7]

[1]Institute of Atmospheric Environment, China Meteorological Administration, Shenyang, China, [2]Center for Analysis and Prediction of Storms, and School of Meteorology, University of Oklahoma, Norman, OK, USA, [3]Department of Occupational and Environmental Health, University of Oklahoma Health Sciences Center, University of Oklahoma, Oklahoma City, OK, USA, [4]Department of Environmental Engineering, Columbia University, New York, NY, USA, [5]Chinese Academy of Meteorological Sciences, China Meteorological Administration, Beijing, China, [6]Shanghai Key Laboratory of Health and Meteorology, Shanghai Meteorological Service, Shanghai, China, [7]GeoCarb Mission, University of Oklahoma, Norman, OK, USA

Abstract CO_2 fluxes and concentrations are not well understood in Northeast China, where dominant land surface types are mixed forest and cropland. Here, we analyzed the CO_2 fluxes and concentrations using observations and the Weather Research and Forecasting model coupled with the Vegetation Photosynthesis and Respiration Model (WRF-VPRM). We also used WRF-VPRM outputs to examine CO_2 transport/dispersion and budgets. Finally, we investigated the uncertainties of simulating CO_2 fluxes related to four VPRM parameters (including maximum light use efficiency, photosynthetically active radiation half-saturation value, and two respiration parameters) using off-line ensemble simulations. The results indicated that mixed forests acted as a larger CO_2 source and sink than rice paddies in 2016 due to a longer growth period and stronger ecosystem respiration, although measured minimum daily mean net ecosystem exchange (NEE) was smaller at rice paddy (-10 μmol·m^{-2}·s^{-1}) than at mixed forest (-6.5 μmol·m^{-2}·s^{-1}) during the growing season (May–September). The monthly fluctuation of column-averaged CO_2 concentrations (XCO_2) exceeded 10 ppm in Northeast China during 2016. The large summertime biogenic sinks offset about 70% of anthropogenic contribution of XCO_2 in this region. WRF-VPRM modeling successfully captured seasonal and episodic variations of NEE and CO_2 concentrations; however, NEE in mixed forest was overestimated during daytime, mainly due to the uncertainties of VPRM parameters, especially maximum light use efficiency. These findings suggest that the WRF-VPRM modeling framework will provide greater understanding of the natural and anthropogenic contributions to the carbon cycle in China, especially after calibration of parameters that control biogenic fluxes.

1. Introduction

Carbon dioxide (CO_2), as one of the major greenhouse gases in the atmosphere, has been considered as a key driver for climate variability and change (Forster et al., 2007; Gregory et al., 2020; Szulejko et al., 2017). Increasing atmospheric CO_2 can produce warmer temperatures in the troposphere and cooler temperatures in the stratosphere, intensify the residual circulation from the equator to the pole, and even modify the chemistry of the future atmosphere (Rind et al., 1990; Seo et al., 2017; Singh et al., 2017). Globally averaged concentrations of atmospheric CO_2 have increased from 280 ppm since the Industrial Revolution (Bauska et al., 2015; Etheridge et al., 1996) to 403.3 ppm in 2016 (WMO, 2017). The growth rate of atmospheric CO_2 concentrations, which represents the additional burden of CO_2 for a given year integrated over all sources and sinks, remained about 2 ppm/year after 2010 (Keenan et al., 2016) but has been as large as 2.96 ppm/year in 2015 due to the tropical outgassing arising from the El Nino (Yue et al., 2017). On the global scale, the ocean and the terrestrial biosphere remove approximately 45% of the CO_2 emitted by human activities each year (Le Quéré et al., 2015), though the interannual variability in the global sink is large. Regional CO_2 sources/sinks have even larger uncertainties. The complex processes and interactions controlling CO_2 uptake/emission by land ecosystems are still not completely understood (Ciais et al., 2019; Reuter et al., 2017; Schimel et al., 2015).

Quantifying the CO_2 uptake by terrestrial ecosystems is significant for understanding the carbon cycle and budget and the real impact of anthropogenic emissions on the growth rate of atmospheric CO_2 concentrations (Dayalu et al., 2018). Various "top-down" and "bottom-up" approaches have been proposed to quantify terrestrial CO_2 fluxes on regional and global scales (Baldocchi et al., 1996; Basu et al., 2018; Knorr, 2000; Piao et al., 2013; Reuter et al., 2017). Atmospheric inversion is a commonly used method that applies an atmospheric transport model to infer the CO_2 fluxes between the land surface and the atmosphere based on in situ-observed and/or satellite-retrieved CO_2 spatiotemporal gradients (e.g., Crowell et al., 2018; Peylin et al., 2013). The inversion method relies on the accuracy of (1) the assumed prior flux field and its error structure, (2) the atmospheric transport modeling, (3) the observational data set assimilated, and (4) the assimilation technique (e.g., Engelen et al, 2004; Ciais et al., 2010). Therefore, there remain large differences among atmospheric-inversion estimates of terrestrial CO_2 fluxes (Basu et al., 2018; Crowell et al., 2019; Peylin et al., 2013; Zhang et al., 2014). Bottom-up methods simulate terrestrial ecosystem CO_2 fluxes using a process- or data-based biosphere model by considering the biochemical mechanisms and physical processes. For example, Tian et al. (2011) used a process-based ecosystem model driven by multiple and complex environmental factors to simulate the net ecosystem exchange (NEE) of CO_2 in China during 1961–2005. However, the environmental process parameters in process-based models are difficult to quantify on different scales (Shi et al., 2018; Zhu et al., 2005), as they are typically validated only at sparse sites over limited ecosystem types. Alternatively, satellite remote sensing presents an opportunity to provide data with global spatial coverage and so evaluates models in a greater variety of conditions. Remote-sensing data-driven models, especially the light use efficiency (LUE) models, have been developed and widely used to simulate the gross ecosystem exchange (GEE) and NEE from ecosystem at regional to global scales. The commonly used LUE models include the Carnegie-Ames-Stanford Approach (Field et al., 1995), Carbon Fix (Veroustraete et al., 2002), Carbon Flux (Turner et al., 2006), the Eddy-Covariance (EC)-LUE model (Yuan et al., 2007), the Vegetation Photosynthesis Model (Xiao et al., 2004), and the Vegetation Photosynthesis and Respiration Model (VPRM) (Mahadevan et al., 2008). GEE and NEE estimated using LUE models still have large uncertainties and discrepancies, mainly due to model structure differences (Yuan et al., 2014) and model parameter choices (Hilton et al., 2013). In general, top-down and bottom-up estimates differ widely across all spatiotemporal scales.

In order to reconcile estimates of NEE using top-down and bottom-up methods, researchers have been incorporating the in situ and satellite observations into modeling studies. The high-temporal-resolution EC measurements of CO_2 fluxes and concentrations over diverse biomes crossing wide latitudes have been widely applied to optimize model parameters and validate modeling results (Dayalu et al., 2018; Hilton et al., 2013; Jamroensan, 2013; Mahadevan et al., 2008; Yuan et al., 2014). In addition, column-averaged CO_2 concentrations (XCO_2) retrieved from satellites are effective to constrain CO_2 fluxes and can be used to evaluate simulation results on wide spatial scales, especially in the regions with limited in situ measurements (Basu et al., 2013; Crowell et al., 2019; Hu et al., 2019b, 2020; Rayner et al., 2014; Rayner & O'Brien, 2001).

CO_2 flux distribution and variation are heavily influenced by meteorological conditions. Previous studies reported that the cyclones (Hurwitz et al., 2004; Zhou et al., 2017), cold fronts (Hu et al., 2019a, 2020), and sea-land (Ahmadov et al., 2007) and lake-land breezes (Diao et al., 2015) resulted in large fluctuations in atmospheric CO_2 fluxes and concentrations and played a major role in regional and global CO_2 transport and budget (Chan et al., 2004; Parazoo et al., 2011). Therefore, it is critical to develop a weather-biosphere fully coupled model to investigate the mutual impacts of different CO_2 sources and meteorological conditions on the spatiotemporal variation of atmospheric CO_2 concentrations. Ahmadov et al. (2007) coupled the VPRM into the Weather Research and Forecasting (WRF) model to simulate terrestrial CO_2 fluxes and their subsequent atmospheric transport in France. The subsequent study indicated that the WRF-VPRM was able to capture the atmospheric CO_2 temporal and spatial distributions and performed better than other global models in simulating diurnal variability of atmospheric CO_2 concentration field (Ahmadov et al., 2009). In the past decade, the application and evaluation of WRF-VPRM mainly focused on North America (Feng et al., 2016; Hu et al., 2019b, 2020; Park et al., 2018; Ye et al., 2017) and Europe (Pillai et al., 2011). The model performances remain unknown in Asia including China due to the lack of observations, as well as model uncertainties due to uncertainties of VPRM parameters in the region (Dayalu et al., 2018; Hilton et al., 2013; Liu et al., 2015; Zhang et al., 2017a). Diao et al. (2015) used

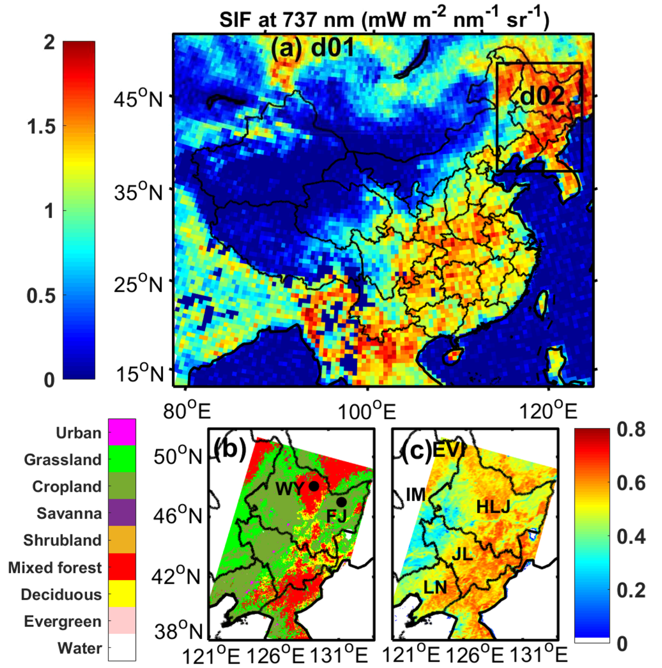

Figure 1. (a) Domain configuration for the WRF-VPRM simulation with the first domain (d01) covering China and the second domain (d02) focusing on Northeast China including four provinces, that is, Heilongjiang (HLJ), Jilin (JL), Liaoning (LN), and the eastern part of Inner Mongolia (IM) Autonomous Region. The background shading shows the spatial distributions of 0.5° × 0.5° summertime (June, July, and August) Sun-induced Fluorescence (SIF) from the Global Ozone Monitoring Experiment-2 (GOME-2) in 2016, (b) dominant vegetation types, and (c) summertime enhanced index vegetation (EVI) in d02 derived from the Moderate Resolution Imaging Spectroradiometer (MODIS) satellite. Black dots represent locations of the rice paddy site in Fujin (FJ) and the mixed forest site in Wuying (WY).

WRF-VPRM to investigate the spatiotemporal characteristics of NEE and surface CO_2 concentrations over the Yangtze River Delta region in China for 5 days, from 28 July to 2 August 2010. Ye et al. (2017) assessed the biotic contribution to the XCO_2 enhancements during two short episodes (12–15 January and 1–4 August 2015) over the Pearl River Delta metropolitan region in China using the WRF-VPRM. However, these short-term (a few days) simulations could not reveal long-term variations of CO_2 fluxes/concentrations. Recently, Dayalu et al. (2018) simulated the NEE over different ecosystems in northern China during the growing seasons (May through September) in 2015–2017 based on the VPRM after optimizing four model parameters using EC measurements and then scaled up regionally using the WRF model in an off-line mode to assess the biotic contributions of atmospheric CO_2 concentrations in this region. Nevertheless, the off-line simulation cannot capture the real-time feedback between synoptic weather and land-surface dynamics and leads to large uncertainties in the simulated CO_2 fluxes/concentrations (Hu, 2008). Liu et al. (2018) reported that surface CO_2 concentrations simulated with the WRF-VPRM exhibited a similar trend with those observed at the Shangdianzi station in Beijing from February to May in 2015. In sum, long-term simulations and observations of CO_2 fluxes/concentrations required to investigate and quantify CO_2 sources/sinks and budget in China are currently rarely reported (He et al., 2019; Thompson et al., 2016; Zhang et al., 2014).

Northeast China (latitudes ranging from 40°–55°N), consisting of provinces of Heilongjiang, Jilin, and Liaoning, as well as the eastern Inner Mongolia Autonomous Region, has two dominant terrestrial ecosystems, cropland and mixed forest (Figure 1b). This region has strong terrestrial CO_2 fluxes in China as indicated by the high Sun-induced Fluorescence (SIF) in summer (June, July, and August) from the Global Ozone Monitoring Experiment-2 (GOME-2) (Fig. 1a). SIF is a direct indicator of photosynthetic activity (Krause & Weis, 1991) and on ecosystem scales has been shown to be proportional to GEE (Sun et al., 2018). Researchers have investigated the seasonal and diurnal variations of CO_2 fluxes using EC measurements over different ecosystems in Northeast China, including rice paddy fields (Jia et al., 2017; Li et al., 2018; Liang et al., 2007), forest regions (Guan et al., 2006; Wang et al., 2008) as well as some less-dominant ecosystems like reed wetlands (Li et al., 2016; Zhou et al., 2009), and freshwater marshes (Yang et al., 2013; Zhang et al., 2005). The EC-measured CO_2 fluxes over rice paddies and mixed forests show a distinct seasonal variation, with the largest CO_2 drawdown (approximately dozens of $\mu mol \cdot m^{-2} \cdot s^{-1}$) occurring in summer due to strong ecosystem photosynthesis while remaining near zero in winter (Guan et al., 2006; Li et al., 2016; Song et al., 2006). Influenced by the seasonal variation of CO_2 fluxes, the satellite-retrieved XCO_2 exhibited higher values in spring and lower values in summer. Due to prominent terrestrial CO_2 fluxes, the XCO_2 in Northeast China exhibited a larger seasonal variation than in other regions in China (Xu et al., 2017; Yang et al., 2016). In addition, CO_2 fluxes exhibited an obvious diurnal variation during the growing season, reaching a maximum sink in the middle of the daytime with a small efflux at night. Previous studies on CO_2 fluxes mostly focused on a specific vegetation type but rarely compared among various dominant ecosystems and rarely examined their overall contribution to total CO_2 budget in Northeast China.

Although researchers have been aware of the potential large impact of terrestrial CO_2 fluxes on atmospheric CO_2 in Northeast China, the detailed spatiotemporal characteristics of CO_2 sources/sinks and budget are still not well understood in this region. Piao et al. (2009) reported that Northeast China was a net source of CO_2 to the atmosphere owing to overharvesting and degradation of forest during 1980s and 1990s. However, Jiang et al. (2016) indicated that the CO_2 uptake by land ecosystems has been increasing after the 1990s in China

Figure 2. Panoramic views of (a) the rice paddy site in Fujin and (b) mixed forest site in Wuying.

because warmer climate and higher levels of atmospheric CO_2 contributed to the increase of productivity in terrestrial ecosystems (Wu et al., 2014). Such a trend has also been reported in the Northern Hemisphere (Ciais et al., 2019) and northern Asia (Peylin et al., 2013). Diao et al. (2006) used an inverse Lagrangian dispersion assimilation technique to constrain the CO_2 source/sink by assimilating data from the Changbai Mountain forest station in Northeast China. However, they only studied one station rather than the whole area of Northeast China.

In this study, we utilize EC measurements, Orbiting Carbon Observatory-2 (OCO-2) satellite data set, and the online WRF-VPRM model to investigate the CO_2 fluxes, concentrations, sources/sinks, and atmospheric CO_2 budget, as well as the impacts of meteorological conditions on CO_2 variations. We also discuss the uncertainties of NEE simulations in relation to the choices of parameters in off-line VPRM simulations.

The rest of this paper is organized as follows. Section 2 introduces observational data and processing procedures and describes the WRF-VPRM model and simulation setup. Section 3 analyzes the seasonal and episodic variations of surface CO_2 fluxes and concentrations in major ecosystems (cropland and mixed forest) in Northeast China and then quantifies biogenic and anthropogenic contributions to XCO_2. We also analyze the diurnal variations of surface CO_2 fluxes and concentrations and model uncertainties of CO_2 fluxes associated with VPRM parameters. Conclusions are summarized in section 4.

2. Methods

2.1. Field Measurements

2.1.1. Site Description

Cropland and mixed forest are major terrestrial ecosystems in Northeast China (Figure 1b). The cropland area in Northeast China was about 215,000 km^2, accounting for 13.3% of the total cropland area in China (Xie et al., 2019). These croplands mostly distributed in plain regions, including the Sanjiang Plain, the Songnen Plain, and the Liaohe Plain. Rice is a major crop in this region, and rice paddy area has been increasing persistently since the 1980s, especially in the Sanjiang Plain (Wu et al., 2014). Forests, particularly mixed forests, cover about 394,500 km^2 area in Northeast China. The forest coverage rate in this region (40%) was more than twice that in China as a whole (16.5%) (Huang, 2019). Mixed forests in Northeast China are mostly located in mountain areas, including the Changbai Mountains, the Da Hinggan Mountains, and the Xiao Hinggan Mountains.

To investigate the CO_2 surface flux and concentration characteristics over dominant vegetation types in Northeast China, two observational stations (Figure 2) were established in Heilongjiang province by the Institute of Atmospheric Environment, China Meteorological Administration in 2012 and 2014, respectively, one in a rice paddy field in Fujin (129.2661°E, 48.2991°N, and 59 m above sea level) and the other one in a mixed forest region in Wuying (131.9385°E, 47.1519°N, and 345 m above sea level) (Figure 1b). The Fujin site was located in the Sanjiang Plain, which has the largest rice production farming region in China (Jia et al., 2018). The Wuying site was located at a national forest park, which remains the largest and well-conserved primitive temperate broad-leaved Korean pine forest in the world (Jia et al., 2018).

2.1.2. Site Observations

EC systems are mounted on a tower at Fujin and Wuying stations to measure turbulence fluctuations of CO_2 concentration, wind speed, and air temperature above the plant canopy with a frequency of 10 Hz (Figure 2). The EC system consists of an open-path CO_2/H_2O analyzer (LI-7500, Li-Cor, Inc., USA), a three-dimensional sonic anemometer (CSAT3, Campbell Scientific, Inc., USA), and a data logger (A755GSM-GPRS, Adcon Telemetry, Germany). The observational height is 3.5 and 40 m above ground level (AGL) at Fujin and Wuying sites, respectively. The EC measurements used in this study were taken in 2016, when data continuity was high. The representativeness of the two stations were evaluated using a footprint analysis method of CO_2 fluxes following Guan et al. (2006). The results showed that approximately 90% of the measured scalar fluxes originated from within 185 and 247 m of the tower at Fujin and Wuying stations, respectively.

In addition, photosynthetically active radiation (PAR) (PAR1, Adcon Telemetry, Germany) is observed at 3.5 m AGL at the Fujin station every 10 min. The PAR data were averaged hourly and then were used to evaluate WRF-VPRM, which employs downwelling shortwave radiation in its parameterization for GEE.

2.1.3. Data Processing

We used the turbulent measurement data to calculate friction velocity (u_*) and NEE in a 30-min interval (Mauder et al., 2008):

$$u_* = \sqrt[4]{\left(-\overline{u'w'}\right)^2 + \left(-\overline{v'w'}\right)^2}, \tag{1}$$

$$NEE = \overline{c'w'}, \tag{2}$$

where u', v' and w' are the fluctuations of wind speed in meridional, zonal, and vertical directions, respectively; c' is the fluctuation of CO_2 concentration.

We followed the quality control method reported by Li et al. (2016) to process the NEE observations. First, we deleted outliers and data with weak turbulence, which often occurs during nighttime and can be distinguished using $u_* < u_{*c}$, where u_{*c} was determined using the method from Zhu et al. (2006) as 0.16 m/s at the rice paddy station (Fujin) and as 0.22 m/s at the mixed forest station (Wuying), respectively. Here, the u_{*c} at Fujin was higher than that estimated at a rice paddy site (0.10 m/s) during 2015 in Panjin, Liaoning province (Li et al., 2018), and the u_{*c} at Wuying was close to that used at a forest site (0.20 m/s) in Changbai Mountain from August 2002 to November 2003 (Guan et al., 2006; Foken & Wichura, 1996). We filled the nighttime gaps based on the fitting equations between the filtered EC-measured NEE and air temperature at night (Li et al., 2016; Zhu et al., 2006). The proportion of filled data to all nighttime data reached about 19.7% at Fujin and 56.4% at Wuying. To avoid the possible impact of filling data on changing the diurnal variation of NEE, the filtered-unfilled data were used for the diurnal variation analysis in this study. For other analysis, the filtered-filled data were used.

2.2. Satellite Observations

2.2.1. OCO-2 Satellite Observations

We used the OCO-2 Version 9 XCO_2 data retrieved from full physics retrieval as detailed in Kiel et al. (2019) to investigate XCO_2 over Northeast China in 2016. The OCO-2 satellite, launched in 2014, collects data in a Sun-synchronous orbit with a local equator overpass time of 1:30 pm. It measures the intensity of reflected sunlight in three wavelength bands (0.76, 1.60, and 2.06 μm), which are used to infer column average dry air mole fractions of CO_2 (typically denoted by XCO_2). In this study, we selected a total of 829 XCO_2 samples (quality flag = 0, representing observations without contamination by clouds) over Northeast China at 12:00 Beijing Time (BT), 13:00 local solar time, throughout 2016 for analyzing the monthly variation of XCO_2 in this region and evaluating that simulated by WRF-VPRM.

2.2.2. MODIS Satellite Observations

The Enhanced Vegetation Index (EVI), which is closely related to the photosynthetic activity, is a major input for the VPRM (Ahmadov et al., 2007). EVI is responsive to canopy structure variations, including leaf area index, canopy type, plant physiognomy, and canopy architecture (Gao et al., 2000). In this study, EVI was calculated from the MOD09A1 C6 500 m 8-day land surface reflectance data set, retrieved from the MODIS satellite (Huete et al., 2002; Zhang et al., 2017b). Figure 1c shows the distribution of summertime averaged EVI in Northeast China in 2016.

In addition, land use types (referred to as plant functional types in Hilton et al., 2013) used in WRF-VPRM to calculate CO_2 fluxes, currently classified into seven categories, namely, evergreen forest, deciduous forest, mixed forest, shrubland, savannah, cropland, and grassland, are also derived from MODIS land cover product (MOD12Q1) (Zhang et al., 2017b).

Table 1
The VPRM Parameter Values Over Seven Vegetation Types Used in This Study

	Crops	Mixed forest	Evergreen forest	Deciduous forest	Shrub	Savanna	Grass
α	0.1300	0.2000	0.1247	0.0920	0.0634	0.2000	0.0515
β	0.5420	0.27248	0.2496	0.8430	0.2684	0.3376	-0.0986
λ	0.085	0.100	0.130	0.100	0.180	0.180	0.115
PAR_0	1074.9	419.50	745.306	514.13	590.7	600.0	717.1

Note. Units are as follows: α, μmol $CO_2 \cdot m^{-2} \cdot s^{-1}$; β, μmol $CO_2 \cdot m^{-2} \cdot s^{-1}$; λ, μmol $CO_2 \cdot m^{-2} \cdot s^{-1}$/μmol $PAR \cdot m^{-2} \cdot s^{-1}$; and PAR_0, μmol $PAR \cdot m^{-2} \cdot s^{-1}$.

2.3. Online Coupled Weather-Biosphere Modeling

2.3.1. WRF-VPRM

VPRM is fully coupled with the WRF model that considers impact of WRF-simulated meteorological fields on calculation of terrestrial CO_2 fluxes every time step and computes transport of CO_2 using simulated continuous meteorological fields (Ahmadov et al., 2007). VPRM simulates NEE as the sum of ecosystem respiration (ER) and GEE (Mahadevan et al., 2008):

$$NEE = ER + GEE. \tag{3}$$

NEE and GEE are defined as the net and gross CO_2 fluxes between the ecosystem and the atmosphere, respectively. ER is CO_2 flux caused by respiration of all organisms, including autotrophic respiration ER_a (caused by vegetation) and heterotrophic respiration ER_h (caused by symbiotic microorganisms in soil). These definitions are based on the view of micrometeorology and take the atmosphere as a reference to determine the flux sign. Flux to the atmosphere increases atmospheric CO_2 mole fraction and is defined to be positive. GEE represents those fluxes caused by plant photosynthesis and thus always has a negative sign, while ER always has a positive sign. NEE and GEE are equivalent to net ecosystem production and gross primary production (GPP) except that Net Ecosystem Production and GPP take the ecosystem as a reference and they have an opposite sign (Chapin et al., 2005). Hereafter, we will only use NEE and GEE. ER and GEE in VPRM are parameterized as

$$ER = (\alpha \times T) + \beta, \tag{4}$$

$$GEE = -\lambda \times T_{scale} \times W_{scale} \times P_{scale} \times \frac{1}{1 + \frac{PAR}{PAR_0}} \times FAPAR_{PAV} \times PAR, \tag{5}$$

where T is the air temperature at 2 m AGL (T_a) in WRF-VPRM simulation and α and β are two empirical parameters. When $T < -\beta/\alpha$, ER is set to zero. GEE depends on more variables, including the maximum LUE λ, temperature scale T_{scale}, water stress scale W_{scale}, phenology scale P_{scale}, PAR, its half-saturation value PAR_0, and the fraction of PAR absorbed by the photosynthetically active portion of the vegetation ($FAPAR_{PAV}$). The $FAPAR_{PAV}$ is proportional to EVI, and here we set $FAPAR_{PAV}$ equal to the MODIS 8-day-updated EVI according to Mahadevan et al. (2008). PAR is calculated using the shortwave (SW) downward radiation as SW/0.505 (Mahadevan et al., 2008). The values of four empirical parameters (α, β, λ, and PAR_0) for seven land use categories used in this study (summarized in Table 1) were calibrated previously by Hilton et al. (2013) using data from 65 EC towers over North America. Note that the calibrated parameters varied between different towers among the same land use category over the North America, and we used the median values from different towers in each category for all the seven categories. The variation of optimal parameters at different locations over the same MODIS-derived land use category may be even larger if they are also calibrated outside of North America, including Northeast China, because the specific soil and plants that fall into each category vary across continents.

2.3.2. Model Setup

Table 2 summarizes the model configurations. WRF-VPRM is configured with two domains including China and nested Northeast China domain (Figure 1a) with a horizontal resolution of 20 and 4 km, respectively. Both model domains have 47 vertical layers extending from the surface to 10 hPa. The simulations ran

Table 2
WRF-VPRM Model Configurations

Reference	Attribute	Model configuration
Dudhia (1989)	Short wave radiation	Dudhia algorithm
Mlawer et al. (1997)	Long wave radiation	Rapid radiative transfer model (RRTM)
Hong et al. (2006)	Boundary layer	Yonsei University (YSU) scheme
Morrison et al. (2009)	Microphysics	Morrison microphysics scheme
Chen and Dudhia (2001)	Land surface model	Noah land-surface scheme
Grell and Devenyi (2002)	Cumulus	Grell-Freitas scheme
Wang and Kotamarthi (2014)	Interior nudging	Spectral nudging
	Nudging variables	Horizontal wind components, temperature, geopotential
	Nudging coefficient	3×10^{-5} s^{-1}
	Nudging height	Above PBL
	Wave number	5 and 3 in the zonal and meridional directions respectively

continuously from 1 January to 31 December 2016 using spectral nudging and climatic downscaling techniques documented by Hu et al. (2017, 2018, 2019b, 2020) and Li et al. (2019). Temperature, geopotential height, and horizontal winds above the boundary layer at a ~1,000 km scale are spectrally nudged to the reanalysis data throughout the downscaling simulation, and variation of these variables over smaller scales are predicted by model dynamics. T_a used to drive VPRM is not directly simulated but diagnosed from temperature at the land surface and the lowest model layers (Hu et al., 2010a), none of which are nudged to the reanalysis data.

The National Center for Environmental Prediction/DOE R2 data (Kanamitsu et al., 2002) provide the meteorological initial and boundary conditions, and the 3° × 2° global CarbonTracker model outputs (version CT2017, released in 2018) provide atmospheric CO_2 initial and boundary conditions (Peters et al., 2007, with updates at https://www.esrl.noaa.gov/gmd/ccgg/carbontracker/). The CT2017 system assimilates in situ CO_2 observations around the world to produce the optimal estimation of global CO_2 fields (CarbonTracker Team, 2018). The CT2017 CO_2 fields have been evaluated and validated by Yuan et al. (2019) and Bernath et al. (2019). The simulations also include anthropogenic and oceanic CO_2 emissions. The 0.1° × 0.1° Open-source Data Inventory for Anthropogenic CO_2 (ODIAC) data set provides the monthly anthropogenic emissions of CO_2, as recommended by Hu et al. (2019a, 2020). The monthly ocean CO_2 fluxes are from a 4° × 5° global ocean climatological database, which includes more than 3 million partial pressure CO_2 measurements (Takahashi et al., 2009). The 0.1° × 0.1° and 4° × 5° emission data are mapped to the modeling domain with a grid spacing of 4 km through spatial interpolation, following a common practice for most simulations with the WRF model with chemistry (WRF-Chem) (Hu et al., 2013, 2014, 2019a; Thomas et al., 2019).

2.4. Parametric Uncertainty Analysis Using Off-Line VPRM

There are reducible and irreducible uncertainties in WRF-VPRM CO_2 simulations. The irreducible uncertainties are attributable to the challenge of accurately quantifying the stochastic variations in atmospheric dynamics (Gilliam et al., 2015; Zhang et al., 2016). The reducible uncertainties are caused by model errors (including the structure error and parametric uncertainties) and biases in model input data (including initial and boundary conditions, as well as emissions). Analyzing reducible uncertainties can assess the accuracy and practical predictability of CO_2 fields and further improve the model performance.

In this study, we focused on examining the parametric uncertainties of VPRM in relation to α, β, λ, and PAR_0, which has a larger impact on the uncertainties in simulated NEE than other variables and parameters used in VPRM (to be discussed in sections 3.1 and 3.5). Since CO_2 does not affect the meteorological variables in the simulations, we examined parameter sensitivities using off-line VPRM simulations with meteorology from the standard WRF-VPRM run and focused on the impact of parametric uncertainties on simulated CO_2 fluxes. In the sensitivity studies, five ensemble simulations (one multiparameter experiment and four single-parameter experiments) were designed following the methods in Nielsen-Gammon et al. (2010), in which the model input parameters were randomly perturbed within reasonable ranges to examine the sensitivity of model outputs to different parameter values. In the multiparameter experiment, we randomly perturbed four parameters simultaneously to examine the uncertainties of NEE simulations due to their

Table 3
Range of VPRM Parameters in Five Groups of Ensemble Simulations

Ensemble simulation	α	β	λ	PAR_0
ES1	[0.12, 0.30]	[0.50, 1.20]	[0.09, 0.14]	[350, 600]
ES2	[0.12, 0.30]	1	0.1	419.5
ES3	0.2	[0.50, 1.20]	0.1	419.5
ES4	0.2	1	[0.09, 0.14]	419.5
ES5	0.2	1	0.1	[350, 600]

parametric uncertainties, while in each single-parameter experiment, we only perturbed one parameter and kept other parameters unchanged to isolate the sensitivities of model outputs due to a single parameter. Similar ensemble simulations have been widely used to analyze uncertainties and predictability in atmospheric chemical transport models in previous studies (e.g., Gneiting & Raftery, 2005; Hu et al., 2010b; Krishnamurti et al., 2000; Nielsen-Gammon et al., 2010; Pinder et al., 2008; Zhang et al., 2007).

In these ensemble simulations, we randomly generated 100 values from a reasonable range for each parameter (see Table 3). The relative range of each VPRM parameter was −40–50% for α, −50–20% for β, −10–40% for λ, and −16.57–43.03% for PAR_0. The variation ranges were located within those obtained at 65 EC sites in North American (see Figure 3 in Hilton et al., 2013) and can likely cover the uncertainties of NEE at the mixed forest station. Second, we ran the multiparameter ensemble simulation (ES1) using the 100 combinations of the four VPRM parameters to calculate the NEE, that is, $NEE_{ES1}(i,t) = f\{\alpha(i), \beta(i), \lambda(i), PAR_0(i), t\}$, with i = 1, 2, ... , 100 and t being the time (different hours in the growing season). In the single-parameter ensemble simulations, ES2, ES3, ES4, and ES5, we ran off-line VPRM using 100 values of one parameter but keeping the other three fixed at the original value (see Table 3). All five experiments were conducted under the growing season of 2016 at the mixed forest station, driven by the WRF-simulated T_a and PAR. Finally, we compared the mean diurnal variation of NEE during the growing season (in terms of the variation range, the mean value, and standard deviation) from ES1–ES5 with the observations and online WRF-VPRM simulation. We also calculated the differences of the growing-season-averaged NEE between each member in ES1–ES5 and WRF-VPRM and attributed these differences to the relative variation ratios of each VPRM parameter.

3. Results

3.1. Seasonal Variations of the NEE and Surface CO_2 Concentrations

Seasonal variations of the NEE and surface CO_2 concentrations at Fujin (rice paddy) and Wuying (mixed forest) stations are first examined (Figures 3a, 3b, 4a, and 4b). At Fujin station, negative daily mean NEEs were observed from mid-June to the end of September. The minimum daily mean NEE of −10 μmol·m^{-2}·s^{-1}

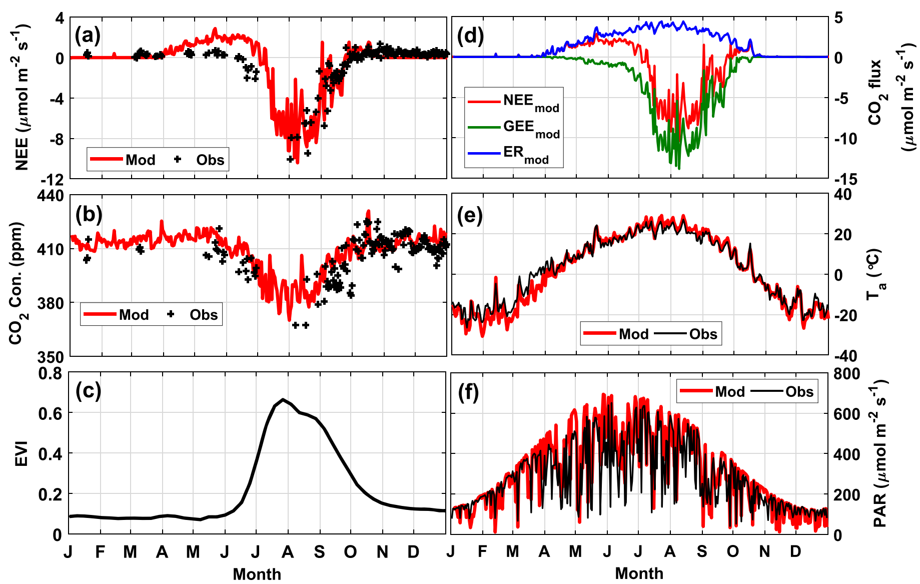

Figure 3. Temporal variations of daily mean observed and simulated (a) net ecosystem exchange (NEE) and (b) surface concentration of CO_2, (c) enhanced vegetation index (EVI) linearly interpolated based on MODIS 8-day-update EVI, (d) simulated NEE, gross ecosystem exchange (GEE), and respiration term (ER), observed and simulated (e) air temperature, and (f) photosynthetically active radiation (PAR) at the rice paddy site in Fujin during 2016.

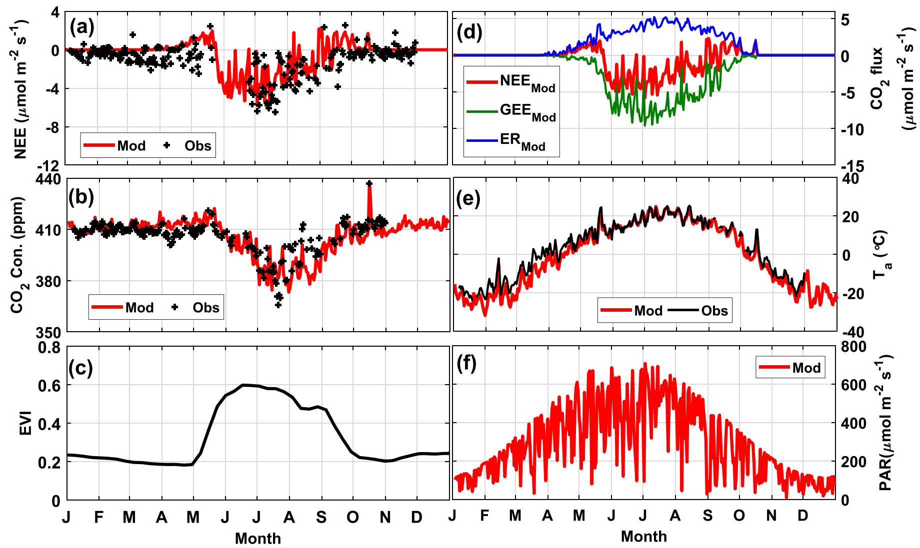

Figure 4. The same as Figure 3 but for the mixed forest site in Wuying without observations of photosynthetically active radiation (PAR).

occurred in the early August. In the nongrowing season, the daily mean NEE mostly exhibited low positive values (<1.5 μmol·m^{-2}·s^{-1}) (Figure 3a). At Wuying station, the NEE started decreasing in mid-May, 1 month earlier than that observed at Fujin, and reached the minimum value of −6.5 μmol·m^{-2}·s^{-1} in July. After reaching the minimum, the NEE increased gradually till the end of September and then varied between ±2.5 μmol·m^{-2}·s^{-1} in the rest time period (Figure 4a). The seasonal variations of NEE and surface CO_2 concentrations at both stations were primarily controlled by EVI (Figures 3c and 4c). With the increase of EVI in summer, the uptake of CO_2 increased due to enhanced ecosystem photosynthesis, resulting in lower surface CO_2 concentrations in summer compared to in other seasons at both stations (Figures 3b and 4b).

These results are consistent with previous studies. For example, the seasonal variation of NEE at Fujin was consistent with that observed at a rice paddy site (41°11′N, 121°54′E) in Liaohe Plain during 2005 (Li et al., 2018) and a rice paddy site (47°35′N, 133°31′E) in Sanjiang Plain during 2004 (Song et al., 2006). Both previous works showed the NEE decreased after mid-June and reached the lowest value in late-July. The observed daily mean NEE in Song et al. (2006) ranged from −13 to 4 μmol·m^{-2}·s^{-1}, which is slightly wider than the range observed at Fujin, though for a different year. The seasonal variation of NEE observed at Wuying was close to the observations at a mixed forest station (42°24′09″N, 128°05′45″E, 738 m) in the Changbai Mountains during 2003 (Guan et al., 2006), in which the daily mean NEE decreased since May and reached the lowest value in late June, ranging from −6.5 to 2.0 μmol·m^{-2}·s^{-1} throughout the year.

WRF-VPRM successfully captured the seasonal variations of NEE and surface CO_2 concentrations at both stations and performed especially well at Fujin (Figures 3a, 3b, 4a, and 4b). During the growing season, the simulated daily mean NEE was similar to the observations at Fujin, with a correlation coefficient (R) of 0.80 and a mean bias of 0.05 μmol·m^{-2}·s^{-1}, and at Wuying, with a R of 0.64 and a mean bias of 0.80 μmol·m^{-2}·s^{-1} (Figure 5). Although the model reproduced NEE at Fujin well in other time periods, it overestimated NEE from April to June. To diagnose the NEE bias, we examined the simulated GEE, ER, and driving meteorological variables including T_a and PAR (Figures 3d–3f and 4d–4f).

The WRF model reproduced the daily variations of T_a throughout the year well, with a R of ≥0.98 between the simulated and observed T_a at both stations. Simulated and observed PAR at Fujin had a R of 0.87. From April to August, PAR at Fujin was overestimated by 78 W/m^2 on average. To isolate the impact of biases of individual meteorological variables (i.e., PAR and T_a) on simulated GEE and NEE, off-line VPRM simulations were conducted with both simulated and observed meteorological variables at the Fujin station throughout 2016 (Figure 6). These off-line VPRM simulations indicated that the biases of PAR had a greater impact on GEE simulations on individual days than the biases of T_a. The uncertainties of simulated GEE caused by the biases of PAR ranged from −5.0 to 3.4 μmol·m^{-2}·s^{-1}, while the uncertainties caused by the

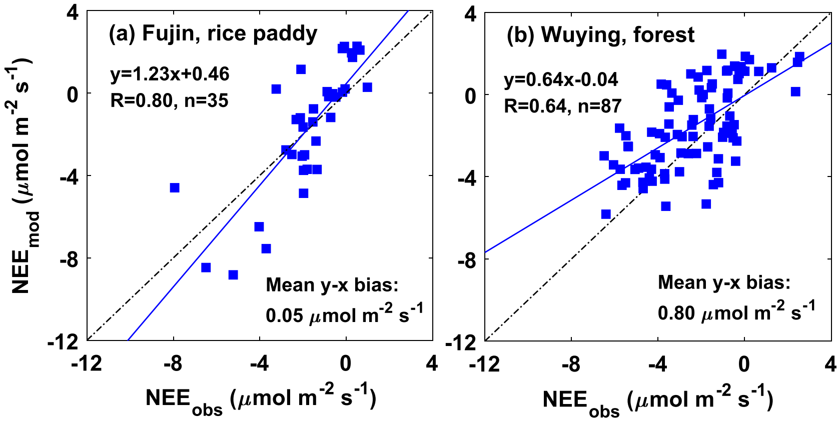

Figure 5. Relationships between observed and simulated daily mean NEE during the growing seasons (from May to September, only on days with observational rate >90%) at (a) the Fujin rice paddy site and (b) the Wuying mixed forest sites. Black line represents the 1:1 line, and blue line represents the fitting equation.

biases of T_a varied between −0.9 and 2.0 μmol·m^{-2}·s^{-1} throughout 2016 at Fujin on individual days. On seasonal or annual scales, the impacts on simulating GEE by PAR or T_a biases were negligible. The biases of PAR and T_a contributed a mean uncertainty of simulated GEE of −0.17 and 0.16 μmol·m^{-2}·s^{-1} during the growing season and of −0.06 and 0.09 μmol·m^{-2}·s^{-1} during the entire year, which was much smaller than that caused by the uncertainties in the four VPRM parameters (reaching −4 μmol·m^{-2}·s^{-1} averaged in the growing season at the most and to be discussed in section 3.5).

In addition to biases in meteorological variables, the NEE modeling bias is also generated from the model errors associated with VPRM itself. Examination of GEE and ER at Fujin station indicates the NEE bias from April to June may be dominantly due to model bias of ER. During April to June, the simulated GEE remained near zero because of low EVI, and meanwhile, the simulated ER increased with the increasing T_a (above 0 °C approximately). In VPRM, while the GEE depends on more variables and is largely dictated by EVI, the ER only linearly depends on T_a. In addition to the linear function used in VPRM, an exponential function between ER and T_a has been suggested to simulate ER (Fang & Moncrieff, 2001; Lloyd & Taylor, 1994). With an exponential parameterization, the increase of ER with T_a becomes relatively slow when T_a is small and gradually enhances with the increase of T_a (Figure S1 in the supporting information). Thus, adopting the exponential parameterization might help to alleviate the bias of simulated ER at least over the rice paddy, particularly in spring with low EVI and increasing T_a. It could also probably produce

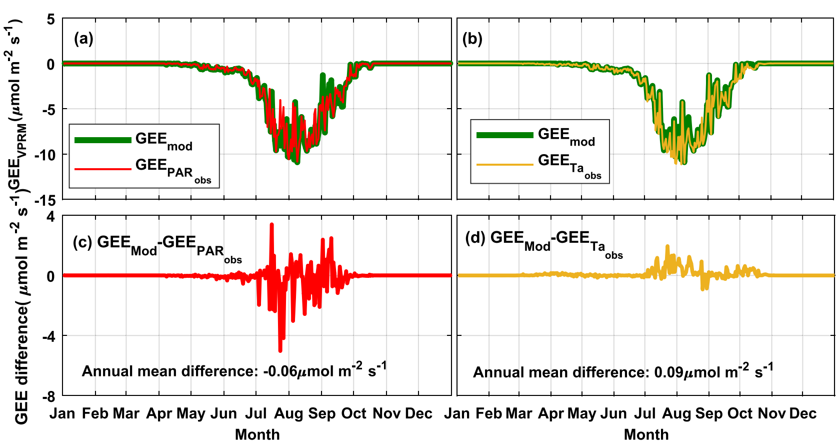

Figure 6. Simulated GEE driven by simulated and observed (a) PAR and (b) T_a and (c and d) the corresponding difference of simulated GEE driven by simulated and observed values.

better results of simulating ER to parameterize plant respiration (which is part of ER) with EVI as well as temperature, since ER depends not only on temperature but also on the mass of leaf and stem of biomes that can be roughly represented by EVI (Guan et al., 2006). The leaf and stem respiration was observed to account for about 27% of the total ER in an old-growth forest area in the Great Lakes region of the Unites States during 2002 and 2003 on average (Tang et al., 2008). A higher proportion (about 52%) was estimated in a temperate mixed forest area in Northeast China (Guan et al., 2006). Therefore, when the EVI was low at Fujin rice station, the values of ER should increase more slowly with T_a due to the limited leaf and stem respiration. These structural deficiency of the VPRM in simulating ER (linear dependency on T_a and not considering EVI) ultimately resulted in an overestimation of NEE at Fujin from April to June. Similar phenomenon also occurred in May at Wuying, but to a less extent.

Setting ER as zero when $T_a \leq -\beta/\alpha$ in current VPRM is another error source in cold seasons (from October to April in Northeast China). Many existing observational studies illustrated that total ER remained above zero in cold seasons. For example, Tang et al. (2008) observed that the wintertime daily mean ER remained about 1 $\mu mol \cdot m^{-2} \cdot s^{-1}$ in an old-growth forest area in the Great Lakes region of the Unites States. Ren et al. (2007) reported that the hourly mean soil respiration ranged from 0.3 to 2.5 $\mu mol \cdot m^{-2} \cdot s^{-1}$ during the nongrowing season in a paddy ecosystem in the subtropical region of China. Mahadevan et al. (2008) adopted different T_{low}, with the T_{low} varying from 1 to 5 °C, for different vegetation types, to calculate ER replacing T_a in presence of $T_a < T_{low}$ for optimal VPRM simulation. We examined the potential optimal T_{low} for VPRM simulation over Fujin. Off-line VPRM simulations were conducted with different T_{low} values (0, 1, 2, and 5°C) at the Fujin station (Figure S2). Simulated daily mean ER increased by 0.1 $\mu mol \cdot m^{-2} \cdot s^{-1}$ approximately with an increase of 1 °C in T_{low} from January to March and from November to December. During the two periods, setting T_{low} as 0 °C could obtain a mean ER value (0.50 $\mu mol \cdot m^{-2} \cdot s^{-1}$) closer to the observed one (0.42 $\mu mol \cdot m^{-2} \cdot s^{-1}$). During warm season, the simulated ER did not depend on T_{low} at most time. In sum, the ER error in cold season is likely due to the VPRM structure errors, which can be reduced by modeling biogenic respiration with more realism.

The uncertainties associated with the VPRM parameters may introduce model bias of GEE. The VPRM parameters for the seven land use categories used in this study were calibrated using data from 65 EC towers over North America. These calibrated parameters even varied among different towers for the same land use category in North America (Hilton et al., 2013); the optimal VPRM parameters over each individual land use category may also vary from North America to Northeast China due to different soil and plants (Diao et al., 2015), even though the same land surface may be chosen using MODIS data. Limited work has been done to optimize the VPRM parameters in China. For example, Liu et al. (2015) and Zhang et al. (2017a) optimized the VPRM parameters at a subtropical evergreen forest site and a mixed forest site in Changbai Mountains, respectively, and the NEE simulations are improved using the optimized VPRM parameters. Dayalu et al. (2018) calibrated the four VPRM parameters for different vegetation types using EC measurements at six stations in China. However, these calibrated VPRM parameters in China have large uncertainties. The uncertainty of simulated NEE due to VPRM parameters will be discussed in section 3.5.

Finally, the biases of simulated GEE by WRF-VPRM may also come from the uncertainty of simple parameterization of GEE as a function of satellite-derived variables, for example, EVI, which may not be a true indicator of total biomass (Matsushita et al., 2007; Shi et al., 2017). In theory, calculating GEE using more accurate estimation of total biomass in process-based models may be more accurate, given that all the involved parameters are carefully calibrated using observations (Farquhar et al., 1980; Pury & Farquhar, 1997; White et al., 2000). However, in most cases, observations are insufficient to calibrate the parameters in more detailed process-based models using more accurate biomass (White et al., 2000), particularly over observation-sparse regions like China. LUE models such as VPRM, even though parameterizing GEE using a crude function of EVI, provide a good compromise between applicability and process details in three-dimensional simulations (Zhang et al., 2017b).

3.2. Episodic Variation of NEE and Surface CO_2 Concentrations on 15 October

Superimposed on the seasonal variation of NEE and surface CO_2 concentrations, a few episodic variations are prominent, which are due to synoptic weather events, such as frontal passages. The highest CO_2

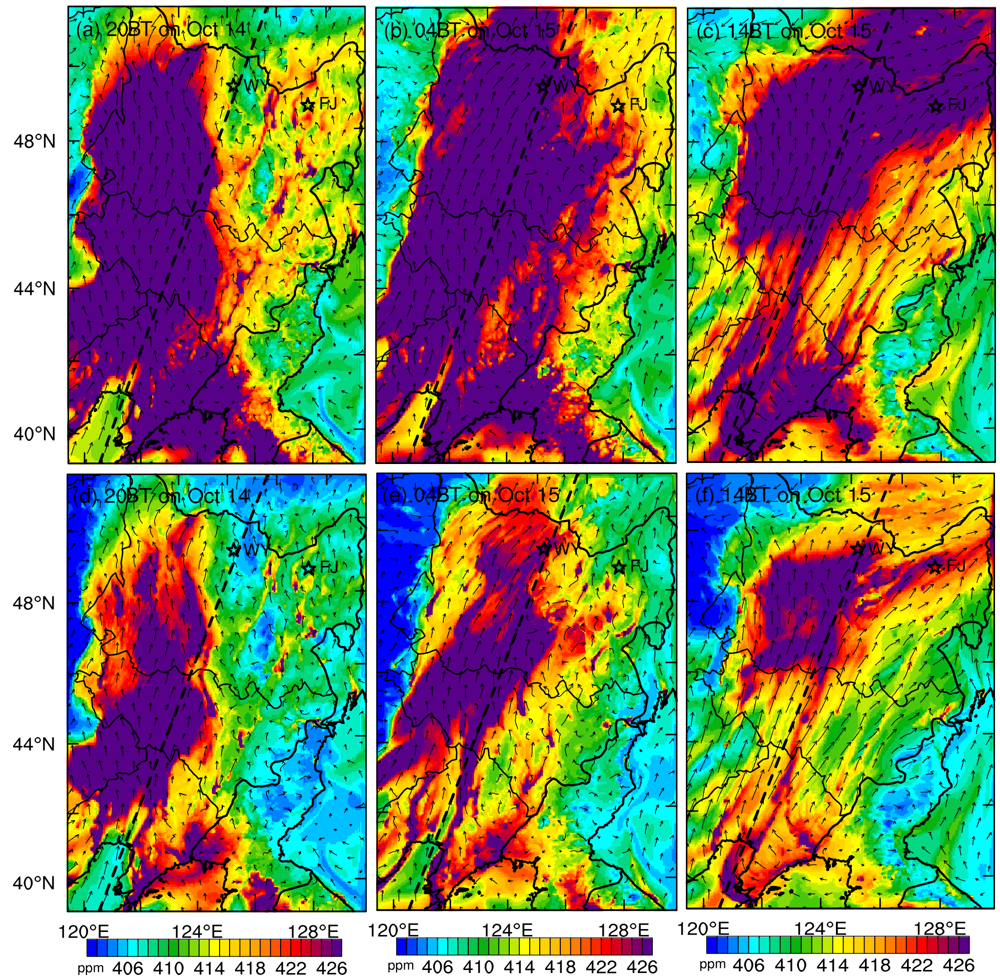

Figure 7. Spatial distributions of simulated surface CO_2 concentrations (including biogenic and anthropogenic contributions) over Northeast China at (a) 20:00 BT on 14 October, (b) 04:00 BT and (c) 14:00 BT on 15 October 2016, and (d–f) those excluding biogenic contribution. Black stars represent the locations of Wuying (WY) and Fujin (FJ) stations. Arrows represent horizontal wind vectors at 10 m AGL.

concentration throughout 2016 with a distinct spike in NEE appeared on 15 October at both Fujin and Wuying. The WRF-VPRM simulation well reproduced the episodic variations at both stations.

We analyzed causes of the high CO_2 episode on 15 October 15. Figure 7 displays the spatial distributions of surface CO_2 concentrations at different time during this episode in Northeast China. The upper three plots are simulation outputs with both anthropogenic emissions and biogenic fluxes, and the bottom three plots are with anthropogenic emissions only. At 20:00 BT on 14 October (Figure 7a), the CO_2 was concentrated in the southern and western regions of Northeast China, where strong southerly flows dominated; thereafter, wind direction turned from the south to the southwest. As a result, CO_2 moved northeastward arriving at Wuying at 04:00 BT on 15 October (Figure 7b) and then Fujin at 14:00 BT on 15 October (Figure 7c). The low-level southwesterly flows can be accelerated by the upper troposphere East Asian subtropical westerly jet, which covered regions with latitudes higher than 40°N, including Northeast China, through downward momentum transport (Kuang et al., 2007; Uccellini & Johnson, 1979). Moreover, local geography can also contribute to the strong southwesterly flows near the surface. The northward moving airflow can be accelerated and tends to have an increase in its anticyclonic vorticity as the Coriolis parameter increases with increasing latitude because of conservation of potential vorticity (Wexler, 1961; Zhong et al., 1996). This means southerly winds from North China Plain, blocked by the southwest-northeast oriented mountains, can become stronger and veer clockwise when arriving at Northeast China (Figure S3). Besides the

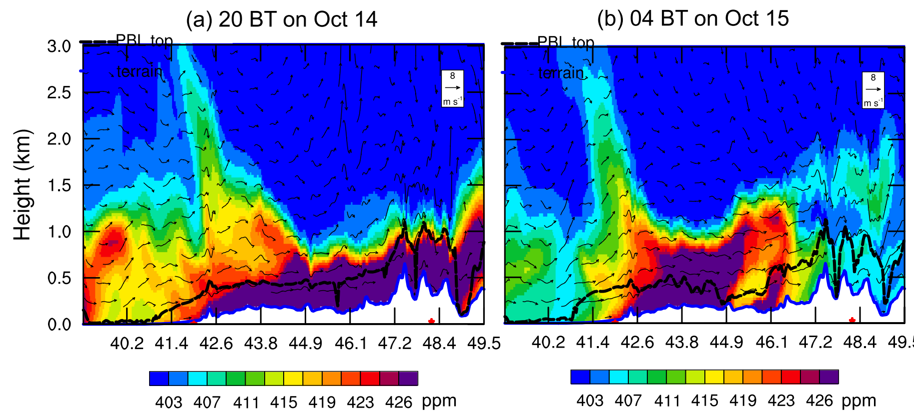

Figure 8. Height-latitude crossing sections of simulated total CO_2 concentration (including biogenic and anthropogenic contributions) along the dash line in Figure 7 at (a) 20:00 BT on 14 October and (b) 04:00 BT on 15 October 2016. The red star represents the location of Wuying station. Arrows represent wind vectors.

horizontal CO_2 transport, subsiding air flows also favored the CO_2 accumulation near the surface (Figure 8). The CO_2 was accumulated in the air under 1 km (Lat. from ~42.0° to ~47.0°) at 20:00 BT on October 14 (Figure 8a). The depth of CO_2-rich layer decreased over time due to strong subsidence between 41–47°N (Figure S4), facilitating farther northeast transport (Figure 8b).

In addition to the favorable meteorological conditions, ER played a significant role in enhancing CO_2 in this episode due to an increase of 7 °C in T_a (see in Figures 3e and 4e). On 15 October, Northeast China was located ahead of a transverse trough, and strong warm advection at low altitudes (at 925 and 850 hPa) favored the abrupt increase in T_a in this region. Without biogenic fluxes, the simulated surface CO_2 concentrations decreased significantly in most region of Northeast China, including Wuying and Fujin (Figures 7d–7f). During this episode, the anthropogenic and biotic fluxes each contributed about 59.4 ± 5.9% and 40.6 ± 5.9% to the increase of surface CO_2 concentrations at Wuying.

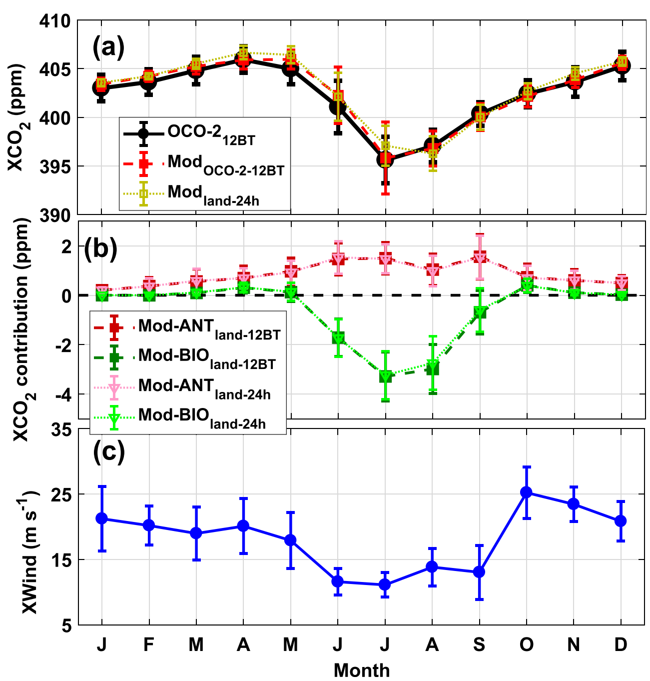

Figure 9. Monthly variations of (a) OCO-2-retreived 12:00 BT XCO_2 (black), correspondingly simulated XCO_2 (red), and 24-hr land-surface averaged XCO_2 (yellow); (b) the simulated 12:00 BT (red) and 24-hr (green) land-surface averaged biogenic and anthropogenic contributions of XCO_2; and (c) the simulated 12:00 BT land-surface averaged column-averaged wind speed in Northeast China during 2016. Error bars represent standard deviation.

3.3. Source Contributions to XCO_2

Radiative/climate forcing is exerted by greenhouse gases in the whole column of the atmosphere, rather than only from the surface. Thus, in addition to near-surface variables, we also examined the total column abundance of CO_2 (XCO_2). We first compare simulations with the OCO-2-retrieved XCO_2 data set to evaluate the performance of WRF-VPRM and then use the model simulations to assess the biogenic and anthropogenic contributions to XCO_2 in Northeast China.

3.3.1. Seasonal Variation of XCO_2

The monthly variation of mean XCO_2 in 2016 over Northeast China was evaluated using data from the OCO-2 satellite (Figure 9a) that has a local overpass time of 1:30 PM (12:30 BT). The simulated XCO_2 at 12:00 BT varied consistently with the OCO-2-retrived XCO_2, with an averaged bias of 0.29 ± 0.48 ppm; both showed the lowest value in July (summer) and the highest value in April (spring). The monthly variation range of both observed and simulated XCO_2 over Northeast China was approximately 10 ppm in 2016 in this study. A slightly larger month variation of XCO_2 (>11 ppm) over the same region was reported by Yang et al. (2016) for 2010 based on the measurements of the Greenhouse gases Observing SATellite. Such a seasonal variation is stronger than that in other regions in China (Xu et al., 2017; Yang et al., 2016). The larger seasonal variation

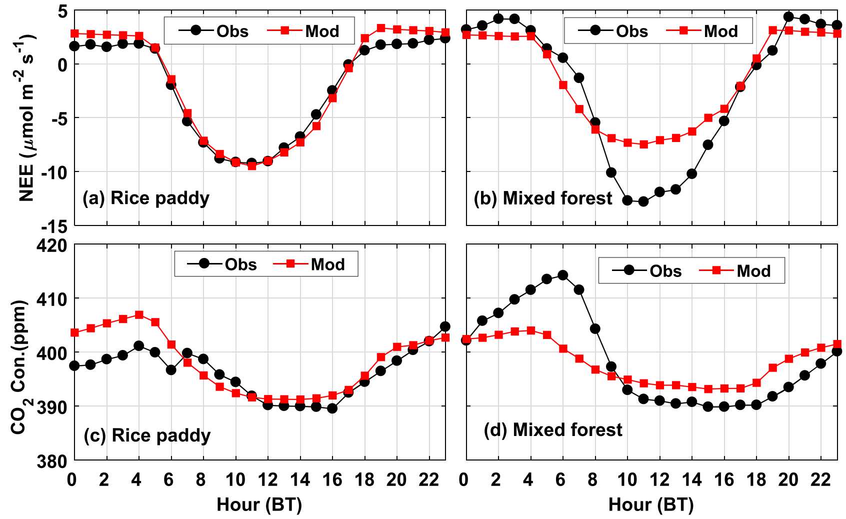

Figure 10. Mean diurnal variations of the observed and simulated (a and b) NEE and (c and d) surface CO_2 concentrations at Fujin rice paddy station and at Wuying mixed forest station during the growing season (May through September) in 2016.

of XCO_2 in Northeast China is caused by significant terrestrial CO_2 fluxes in the region (Yang et al., 2016) and enhanced north-to-south XCO_2 gradient on a larger scale in North Hemisphere in summer (Yang et al., 2018).

3.3.2. Anthropogenic and Biogenic Contributions to XCO_2

Using the WRF-VPRM simulation, we estimated the monthly contributions to XCO_2 from different sources, including anthropogenic emissions and biogenic and oceanic fluxes, averaged over land surface of Northeast China (Figure 9b). Oceanic contribution from nearby Chinese oceans was negligible, two orders smaller in magnitude than anthropogenic and biogenic contributions, thus is not shown in Figure 9. The monthly mean anthropogenic and biogenic contribution at 12:00 BT and over 24 hr are virtually the same, even for biogenic fluxes that have a prominent diurnal variation in the growing season. While diurnal variation of biogenic flux generally follows diurnal variation of radiation, thus reaching maximum uptake flux during noon time (Figure 10), diurnal variation of its contribution to XCO_2 lags behind by ~5 hr, showing a maximum drawdown of XCO_2 around 17:00 BT during the growing season (Figure S5), similar as previously reported by Olsen and Randerson (2004). As a result of such a diurnal variation, biogenic contribution to XCO_2 at 12:00 BT roughly equals its contribution over the whole day.

Anthropogenic emissions contributed 0.21–1.54 ppm to XCO_2 in each month, with contribution during summer months being three times larger than the annual mean contribution. The seasonal variation of ODIAC anthropogenic emissions averaged in Northeast China was from 0.65 to 0.83 $\mu mol \cdot m^{-2} \cdot s^{-1}$ (not shown). During June–September, the mean anthropogenic emission (0.745 $\mu mol \cdot m^{-2} \cdot s^{-1}$) was 2% higher than the annual mean of 0.738 $\mu mol \cdot m^{-2} \cdot s^{-1}$, which cannot explain a threefold increase of anthropogenic contribution of XCO_2 during summer months comparing with the annual mean contribution. Instead, the monthly variation of winds likely dictated the monthly variation of anthropogenic contribution. The column-averaged wind speed (denoted as XWind, computed similarly as XCO_2) from June to September in Northeast China was observed 32% lower than the annual mean level (Figure 9c). The weak winds in summer favored the accumulation of CO_2 within local areas.

Terrestrial ecosystems acted as a CO_2 sink from June to September in Northeast China, contributing −3.22 to −0.60 ppm to XCO_2. Terrestrial ecosystems contributed insignificantly to XCO_2 in other months (<0.39 ppm). The annual mean biogenic contributions to XCO_2 in Northeast China in 2016 was estimated to be −0.60 ppm, which offsets 71% of the annual mean positive anthropogenic contribution (0.84 ppm).

3.4. Diurnal Variations of NEE and Surface CO_2 Concentrations

Source and sinks of CO_2 at regional to continental scales remain poorly understood. Even though multiple GPP products on daily scales (usually 8-day) are available, their performances vary substantially when

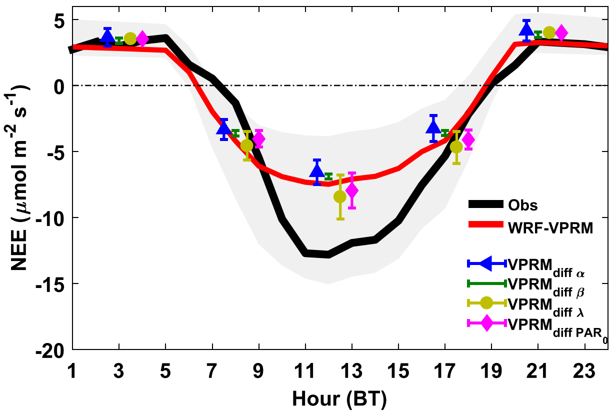

Figure 11. Mean diurnal variation of the NEE spread during the growing season (May through September) in 2016 from multiparameter ensemble simulation (ES1, shaded area) and mean and standard deviation (error bars) values of NEE from single-parameter simulations (α, triangle; β, line; λ, circle; and PAR_0, diamond) at Wuying mixed forest station at 03:00, 08:00, 12:00, 17:00, and 21:00 BT. Thick black line represents observed NEE at Wuying site, and gray line represents simulated NEE with WRF-VPRM.

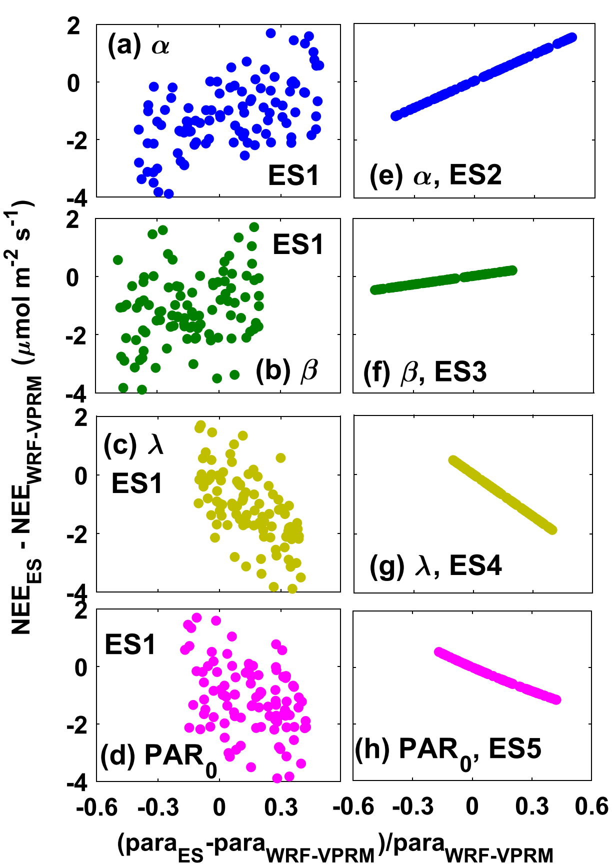

Figure 12. Scattering plots of differences between the growing-season-averaged NEE values for each member in ensemble simulations and that simulated with WRF-VPRM at Wuying against relative variation ratio of VPRM parameters (including α, β, λ, and PAR_0). (a–d) multiparameter ensemble simulations (ES1); (e–h) single-parameter simulation (ES2–ES5).

validated against EC observations (Zhang et al., 2017b). This is at least partly due to our limited understanding on the photosynthesis and respiration processes, including their diurnal variations. Better estimation of total NEE has to be achieved through better understanding of its diurnal variation and better parameterization of diurnal variations of the photosynthesis and respiration processes. Diurnal variation of CO_2 fluxes and concentration was examined below.

The observed diurnal variation pattern of NEE and surface CO_2 concentrations at Fujin and Wuying (Figure 10) was consistent with previous observations (Bazzaz & Williams, 1991; Guan et al., 2006; Park et al., 2018; Song et al., 2006; Zhang et al., 2017a). The negative NEE occurred between 06:00 and 17:00 BT, with the lowest value at the middle of the day, while the surface CO_2 concentration began to increase after sunset, reached a peak in the early morning, and then decrease till 18:00 BT at both stations.

The observed mean diurnal variation of NEE in the growing season exhibited a wider range in mixed forest (from −12.8 to 3.6 $\mu mol \cdot m^{-2} \cdot s^{-1}$ at Wuying; see Figure 10b) than the rice paddy field (from −9.2 to 2.2 $\mu mol \cdot m^{-2} \cdot s^{-1}$ at Fujin; see Figure 10a). This suggests mixed forests acted as a larger CO_2 sink/source than rice paddies in 2016 due to a longer growth period and stronger ER, although the canopy photosynthesis and hence the peak CO_2 sink were stronger in rice paddies in June and July (Figures 3a and 4a). These differences corroborate previous understanding that terrestrial ecosystems with the greatest net carbon uptake usually have the longest growing season, rather than the greatest canopy photosynthesis (Baldocchi, 2008). The nighttime EC-measured NEE at Wuying (>3 $\mu mol \cdot m^{-2} \cdot s^{-1}$) was larger than that at Fujin (<2 $\mu mol \cdot m^{-2} \cdot s^{-1}$) likely because of stronger soil respiration in forest than that in rice paddy (Brændholt et al., 2018; Ren et al., 2007; Tang et al., 2008), as well as stronger leaf and stem respiration in forests than in rice paddies due to the difference in biomass. The mean EVI during the growing season at Wuying was approximately 30% higher than that at Fujin in 2016 (Figures 3c and 4c). The growing-season mean diurnal variation of surface CO_2 concentration at Wuying also exhibited a wider range than that at Fujin (Figures 10b and 10d), which is partially due to larger CO_2 fluxes at mixed forest.

Different from many previous LUE model investigations that examined daily mean surface CO_2 fluxes (Running et al., 2004; Xiao et al., 2008; Zhang et al., 2017b), our online WRF-VPRM simulation calculates CO_2 fluxes and three-dimensional CO_2 fields every time step. Thus, we can examine CO_2 fluxes and concentrations on a subdaily time scale using WRF-VPRM outputs and examine model errors on short time scales that have not been thoroughly discussed before (Diao et al., 2015; Zhang et al., 2017a). WRF-VPRM well reproduced the daytime NEE and surface CO_2 concentration at Fujin but slightly overestimated their nighttime values (Figures 10a and 10c). At Wuying, the model overestimated the daytime NEE by approximately 9% (~2.25 $\mu mol \cdot m^{-2} \cdot s^{-1}$) and underestimated the nighttime NEE by 38% (~0.66 $\mu mol \cdot m^{-2} \cdot s^{-1}$) on average (Figure 10b). As a result, the diurnal variation range of surface CO_2 concentrations at Wuying was also underestimated (Figure 9d). Zhang et al. (Zhang et al., 2017a) also reported an underestimation on diurnal variation of NEE simulated with VPRM in the growing season in a mixed

Table 4
Values of Maximum Light Use Efficiency λ Optimized Over Different Mixed Forests in Previous Studies

Reference	Site location	Observational year	Values of λ
Hilton et al. (2013)	North America	2007	0.20
Zhang et al. (2017)	Changbaishan, Northeast China	2015	0.315
Dayalu et al. (2018)	Changbaishan, Northeast China	2015	0.123
Yuan et al. (2013)	Global 9 sites	—	2.03 ± 0.24
Mahadevan et al. (2008)	Massachusetts, United State	2000–2003	0.127
Mahadevan et al. (2008)	Maine, United State	2000–2003	0.123

forest region of the Changbai Mountains using default VPRM parameters from Mahadevan et al. (2008). In order to understand the model performance at Wuying, we conducted off-line VPRM sensitivity simulations to understand the uncertainty of NEE simulation in relation to the selection of VPRM parameters in the next section.

3.5. Parametric Uncertainty Analysis of NEE Simulations Using Off-Line VPRM

We conducted five experiments with off-line VPRM ensemble simulations (ES1–ES5, designed in section 2.4) at Wuying during the growing season of 2016 to investigate the uncertainty of NEE simulations in relation to the choices of VPRM parameters. The sensitivity of NEE in the daytime was larger than at nighttime. The NEE ranges in multiparameter run (ES1) covered the observed NEE at all hours during the growing season, showing that the WRF-VPRM is able to predict the observed NEE through adjusting the VPRM parameters. The results of ES2–ES5 suggested that the nighttime NEE depended more on α than on β; while the daytime NEE depended more on λ and PAR_0 than on two respiration parameters (Figure 11).

The sensitivity of NEE to each VPRM parameter is shown in Figure 12. We calculated the differences between the growing-season averaged NEE for each member from ES1–ES5 and from the WRF-VPRM simulation. Figure 12 shows the relationships of these NEE differences against the relative variation ratio of each VPRM parameter. In ES1, the NEE differences exhibited strong negative correlations with variation of λ and PAR_0, a weak positive correlation for α, and no obvious correlation for β. This means during the growing season, photosynthesis process dominantly controlled the NEE. In ES2–ES5, the NEE difference was most sensitive to λ, followed by PAR_0, α, and β. This means a small change of λ can lead to a considerable variation of simulated NEE.

The λ is commonly known as an important parameter to calculate GEE and then NEE in the VPRM (Liu et al., 2015); however, the literature shows a large range of possible values (see Table 4). The large uncertainties and diversities of estimates of λ are due to the difference in climatic environment at different observational sites, data processing procedure, and driving data used. Such parametric uncertainties in WRF-VPRM can be probably reduced by more detailed classification of land use based on MODIS data and calibrating these VPRM parameters over these more detailed land use categories, given that more detailed land classification based on MODIS data is reliable and tower data are available for the detailed land use classification. However, currently, both the prerequirements for such improvement of WRF-VPRM (i.e., more detailed land use classification based on MODIS and tower data over each detailed land use classification) are not very realistic, particularly over Northeast China where tower data are very sparse. Under such circumstances, ensemble simulations help to predict a better range of NEE as long as a reasonable range for each parameter can be provided. The sensitivity analysis based on ensemble simulations also provides guidance for future studies, suggesting that the best parameter to optimize would be λ. Global optimization of VPRM parameters is beyond the scope of the current project but should be revisited in the future.

4. Conclusions

Northeast China is dominated by mixed forest and cropland with prominent terrestrial CO_2 fluxes. Long-term CO_2 fluxes and their impacts on CO_2 concentrations are poorly understood for this region. In this study, the terrestrial CO_2 fluxes and concentrations in Northeast China during 2016 are analyzed using (1) field measurements at a rice paddy site in Fujin and a mixed forest site in Wuying, (2) satellite observations, and (3) the online WRF-VPRM simulation. To the best of our knowledge, the present work is the first one to study the CO_2 sources/sinks and budget in Northeast China using an online WRF-VPRM simulation together with field and satellite observations.

The seasonal variations of NEE and surface CO_2 concentrations were first examined. Negative NEE (i.e., uptake of CO_2), corresponding to high EVI, mostly occurred from mid-July to September at the Fujin rice station, and from May to September at the Wuying forest station. The lowest daily mean NEE occurred in August with −10 μmol·m^{-2}·s^{-1} at Fujin, and in July with −6.5 μmol·m^{-2}·s^{-1} at Wuying, respectively. During the nongrowing season, when the EVI was low, the NEE remained negligible at both stations. The seasonal variations of surface CO_2 concentrations were greatly influenced by terrestrial CO_2 fluxes, with the lowest value in summer. WRF-VPRM reproduced the seasonal variations of NEE and surface CO_2 concentrations, with a better performance at Fujin than Wuying. The NEE at Wuying was overestimated on average during the growing season (May through September) due to the overestimation of GEE. VPRM does not consider the impact of biomass on respiration and sets ER as zero when $T_a < -\beta/\alpha$, which should be improved in the future. Notwithstanding, the WRF-VPRM also successfully captured a high surface CO_2 episode in the nongrowing season on October 15. This episode occurred due to the transport of CO_2 by strong southwesterly winds and subsidence as well as enhanced local biotic respiration due to an abrupt increase in T_a.

In addition to near-surface variables, we also examined the total column abundance of CO_2 (XCO_2). The simulated monthly XCO_2 by WRF-VPRM was comparable to the OCO-2 observations, with the lowest value (395 ppm) in summer and the highest value (406 ppm) in spring. The annual anthropogenic and biogenic contributions to XCO_2 over Northeast China in 2016 were estimated to be approximately 0.84 and −0.60 ppm, respectively, based on WRF-VPRM outputs.

The mean diurnal variations of NEE and surface CO_2 concentrations were examined at Fujin and Wuying during the growing season. The mean diurnal variation ranges of NEE and surface CO_2 concentrations were larger at Wuying than at Fujin because of stronger ER and longer growth period of mixed forest compared to those of rice paddy. WRF-VPRM reproduced the daytime NEE and CO_2 concentrations at Fujin well but slightly underestimated their nighttime value by 1.05 μmol·m^{-2}·s^{-1}, on average. The model significantly underestimated the diurnal variation ranges of NEE and surface CO_2 concentrations at Wuying forest station.

To investigate the uncertainties of VPRM parameters in relation to NEE error over Wuying, one multiparameter (ES1) and four single-parameter (ES2–ES5) ensemble simulations were conducted for the growing season with off-line VPRM. The variation range of simulated NEE in ES1 enveloped the observed NEE at all hours during the growing season. The nighttime NEE was more sensitive to α than β, while the daytime NEE was most sensitive to λ. As a major source for the reducible uncertainties in WRF-VPRM, the uncertainties in the four VPRM empirical parameters can be reduced through optimization using more observational data in the studied region. Given the current uncertainties of these parameters, ensemble simulation perturbing the parameters in their plausible range is another method to capture the range of NEE and subsequent CO_2 transport and dispersion.

Acknowledgments
This work was jointly supported by the National Nature Science Foundation of China (41405109 and 41605081), National Key Research and Development Program of China (2018YFC1506802), and Basic Research Funds of Central Public Welfare Research Institutes (2017SYIAEMS2 and 2018SYIAEZD3). The second author was supported by NASA Grant NNX17AG11G. Sean Crowell is partially funded by the OCO-2 External Science Team under Grant 80NSSC18K0896. Computations were performed at the San Diego Supercomputer Center (SDSC) through XSEDE Allocation Grant TG-ATM160014. We thank the group of Drs. Xiangming Xiao and Cheng Liu for discussing the results of EC measurements and the VPRM simulation. OCO-2 XCO_2 data were downloaded online (from https://co2.jpl.nasa.gov/#mission=OCO-2). Other data used by this study have been archived at the oasis data server at the San Diego Supercomputer Center (/oasis/projects/nsf/uok114/leexl/CO2paper).

Reference

Ahmadov, R., Gerbig, C., Kretschmer, R., Koerner, S., Neininger, B., Dolman, A. J., & Sarrat, C. (2007). Mesoscale covariance of transport and CO_2 fluxes: Evidence from observations and simulations using the WRF-VPRM coupled atmosphere-biosphere model. *Journal of Geophysical Research*, *112*(D22), D22107. http://doi.org/10.1029/2007jd008552

Ahmadov, R., Gerbig, C., Kretschmer, R., Körner, S., Rödenbeck, C., Bousquet, P., & Ramonet, M. (2009). Comparing high resolution WRF-VPRM simulations and two global CO_2 transport models with coastal tower measurements of CO_2. *Biogeosciences*, *6*(5), 807–817. http://doi.org/10.5194/bg-6-807-2009

Baldocchi, D. (2008). 'Breathing' of the terrestrial biosphere: Lessons learned from a global network of carbon dioxide flux measurement systems. *Australian Journal of Botany*, *56*(1), 1–26. https://doi.org/10.1071/BT07151

Baldocchi, D., Valentini, R., Running, S., Oechel, W., & Dahlman, R. (1996). Strategies for measuring and modelling carbon dioxide and water vapour fluxes over terrestrial ecosystems. *Global Change Biology*, *2*(3), 159–168. https://doi.org/10.1111/j.1365-2486.1996.tb00069.x

Basu, S., Baker, D. F., Chevallier, F., Patra, P. K., Liu, J., & Miller, J. B. (2018). The impact of transport model differences on CO_2 surface flux estimates from OCO-2 retrievals of column average CO_2. *Atmospheric Chemistry and Physics*, *18*, 7189–7215. https://doi.org/10.5194/acp-18-7189-2018

Basu, S., Guerlet, S., Butz, A., Houweling, S., Hasekamp, O., Aben, I., et al. (2013). Global CO_2 fluxes estimated from GOSAT retrievals of total column CO_2. *Atmospheric Chemistry and Physics*, *13*(17), 8695–8717. http://doi.org/10.5194/acp-13-8695-2013

Bauska, T. K., Joos, F., Mix, A. C., Roth, R., Ahn, J., & Brook, E. J. (2015). Links between atmospheric carbon dioxide, the land carbon reservoir and climate over the past millennium. *Nature Geoscience*, *8*(5), 383–387. https://doi.org/10.1038/

Bazzaz, F. A., & Williams, W. E. (1991). Atmospheric CO_2 concentrations within a mixed forest: Implications for seedling growth. *Ecology*, *72*(1), 12–16. http://doi.org/10.2307/1938896

Bernath, P., Boone, C., Fernando, A., & Jones, S. (2019). Low altitude CO_2 from the Atmospheric Chemistry Experiment (ACE) Satellite. *Journal of Quantitative Spectroscopy and Radiative Transfer*, *238*, 106528. https://doi.org/10.1016/j.jqsrt.2019.06.007

Brændholt, A., Ibrom, A., Larsen, K. S., & Pilegaard, K. (2018). Partitioning of ecosystem respiration in a beech forest. *Agricultural and Forest Meteorology*, *252*, 88–98. http://doi.org/10.1016/j.agrformet.2018.01.012

CarbonTracker Team, 2018. CarbonTracker Documentation CT2017 release. https://www.esrl.noaa.gov/gmd/ccgg/carbontracker/CT2017_doc.php#tth_sEc1.3

Chan, D., Yuen, C. W., Higuchi, K., Shashkov, A., Liu, J., Chen, J., & Worthy, D. (2004). On the CO_2 exchange between the atmosphere and the biosphere: The role of synoptic and mesoscale processes. *Tellus Series B: Chemical and Physical Meteorology*, *56*(3), 194–212. http://doi.org/10.1111/j.1600-0889.2004.00104.x

Chapin, F. S. III, Woodwell, G. M., Randerson, J. T., Rastetter, E. B., Lovett, G. M., Baldocchi, D. D., et al. (2005). Reconciling carbon-cycle concepts, terminology, and methodology. *Ecosystems*, *9*, 1041–1050. https://doi.org/10.1007/s10021-005-0105-7

Chen, F., & Dudhia, J. (2001). Coupling an advanced land surface-hydrology model with the Penn State-NCAR MM5 modeling system. Part I: Model implementation and sensitivity. *Monthly Weather Review*, *129*(4), 569–585. https://doi.org/10.1175/1520-0493(2001)129<0569:Caalsh>2.0.Co;2

Ciais, P., Rayner, P., Chevallier, F., Bousquet, P., Logan, M., Peylin, P., & Ramonet, M. (2010). *Atmospheric inversions for estimating CO_2 fluxes: Methods and perspectives*. Springer, Dordrecht: Greenhouse Gas Inventories.

Ciais, P., Tan, J., Wang, X., Roedenbeck, C., Chevallier, F., Piao, S. L., et al. (2019). Five decades of northern land carbon uptake revealed by the interhemispheric CO_2 gradient. *Nature*, *568*(7751), 221–225. http://doi.org/10.1038/s41586-019-1078-6

Crowell, S., Baker, D., Schuh, A., Basu, S., Jacobson, A. R., Chevallier, F., et al. (2019). The 2015–2016 carbon cycle as seen from OCO-2 and the global in situ network. *Atmospheric Chemistry and Physics*, *19*(15), 9797–9831. https://doi.org/10.5194/acp-2019-87

Crowell, S. M., Randolph Kawa, S., Browell, E. V., Hammerling, D. M., Moore, B., Schaefer, K., & Doney, S. C. (2018). On the ability of space-based passive and active remote sensing observations of CO_2 to detect flux perturbations to the carbon cycle. *Journal of Geophysical Research*, *123*(2), 1460–1477. http://doi.org/10.1002/2017JD027836

Dayalu, A., Munger, J. W., Wofsy, S. C., Wang, Y., Nehrkorn, T., Zhao, Y., et al. (2018). Assessing biotic contributions to CO_2 fluxes in northern China using the Vegetation, Photosynthesis and Respiration Model (VPRM-CHINA) and observations from 2005 to 2009. *Biogeosciences*, *15*(21), 6713–6729. http://doi.org/10.7910/DVN/RQLGLH

Diao, Y., Huang, J., Liu, C., Cui, J., & Liu, S. (2015). A modeling study of CO_2 flux and concentrations over the Yangtze River Delta using the WRF-GHG model. *Chinese Journal of Atmospheric Sciences*, *39*(5), 849–860. http://doi.org/10.3878/j.issn.1006-9895.1409.14127 (in Chinese)

Diao, Y., Wang, A., Guan, D., Jin, C., & Pei, T. (2006). Modeling CO_2 source-sink and flux over broadleaved Koreanpine forest in Changbai Mountain using inverse Lagrangian dispersion analysis. *Journal of Geophysical Research-Atmospheres*, *111*, D15S90. https://doi.org/10.1029/2005JD006493

Dudhia, J. (1989). Numerical study of convection observed during the winter monsoon experiment using a mesoscale two-dimensional model. *Journal of the Atmospheric Sciences*, *46*(20), 3077–3107. https://doi.org/10.1175/1520-0469(1989)046<3077:Nsocod>2.0.Co;2

Etheridge, D. M., Steele, L. P., Langenfelds, R. L., Francey, R. J., Barnola, J.-M., & Morgan, V. I. (1996). Natural and anthropogenic changes in atmospheric CO_2 over the last 1000 years from air in Antarctic ice and firn. *Journal of Geophysical Research*, *101*(D2), 4115–4128. http://doi.org/10.1029/95JD03410

Fang, C., & Moncrieff, J. B. (2001). The dependence of soil CO_2 efflux on temperature. *Soil Biology and Biochemistry*, *33*(2), 155–165. http://doi.org/10.1016/S0038-0717(00)00125-5

Farquhar, G. D., von Caemmerer, S. V., & Berry, J. A. (1980). A biochemical model of photosynthetic CO_2 assimilation in leaves of C3 species. *Planta*, *149*(1), 78–90. https://doi.org/10.1007/BF00386231

Feng, S., Lauvaux, T., Newman, S., Rao, P., Ahmadov, R., Deng, A., et al. (2016). Los Angeles megacity: A high-resolution land-atmosphere modelling system for urban CO_2 emissions. *Atmospheric Chemistry and Physics*, *16*, 9019–9045. https://doi.org/10.5194/acp-16-9019-2016

Field, C. B., Randerson, J. T., & Malmström, C. M. (1995). Global net primary production: Combining ecology and remote sensing. *Remote Sensing of Environment*, *51*(1), 74–88. http://doi.org/10.1016/0034-4257(94)00066-V

Foken, T., & Wichura, B. (1996). Tools for quality assessment of surface-based flux measurements. *Agricultural and Forest Meteorology*, *78*(1-2), 83–105. https://doi.org/10.1016/0168-1923(95)02248-1

Forster, P., Ramaswamy, V., Artaxo, P., Berntsen, T., Betts, R., Fahey, D. W., et al. (2007). Changes in atmospheric constituents and in radiative forcing, in Climate Change 2007: The Physical Science Basis. In S. Solomon, et al. (Eds.), *Contribution of Working Group I to the Fourth Assessment Report of the Intergovernmental Panel on Climate Change* (pp. 131). New York: Cambridge University Press.

Gao, X., Huete, A. R., Ni, W., & Miura, T. (2000). Optical-biophysical relationships of vegetation spectra without background contamination. *Remote Sensing of Environment*, *74*(3), 609–620. http://doi.org/10.1016/S0034-4257(00)00150-4

Gilliam, R. C., Hogrefe, C., Godowitch, J. M., Napelenok, S., Mathur, R., & Rao, S. T. (2015). Impact of inherent meteorology uncertainty on air quality model predictions. *Journal of Geophysical Research-Atmospheres*, *120*(23), 12–259. https://doi.org/10.1002/2015JD023674

Gneiting, T., & Raftery, A. E. (2005). Weather forecasting with ensemble methods. *Science*, *310*(5746), 248–249. http://doi.org/10.1126/science.1115255

Gregory, J. M., Andrews, T., Ceppi, P., Mauritsen, T., & Webb, M. J. (2020). How accurately can the climate sensitivity to CO_2 be estimated from historical climate change? *Climate Dynamics*, *54*(1-2), 129–157. https://doi.org/10.1007/s00382-019-04991-y

Grell, G. A., & Devenyi, D. (2002). A generalized approach to parameterizing convection combiningensemble and data assimilation techniques. *Geophysical ResearchLetters*, *29*(14), 1693. https://doi.org/10.1029/2002gl015311

Guan, D. X., Wu, J. B., Zhao, X. S., Han, S. J., Yu, G. R., Sun, X. M., et al. (2006). CO_2 fluxes over an old, temperate mixed forest in northeastern China. *Agricultural and Forest Meteorology*, *137*(3–4), 138–149. http://doi.org/10.1016/j.agrformet.2006.02.003

He, H., Wang, S., Zhang, L., Wang, J., Ren, X., Zhou, L., et al. (2019). Altered trends in carbon uptake in China's terrestrial ecosystems under the enhanced summer monsoon and warming hiatus. *National Science Review*, *6*(3), 505–514. https://doi.org/10.1093/nsr/nwz021

Hilton, T. W., Davis, K. J., Keller, K., & Urban, N. M. (2013). Improving North American terrestrial CO_2 flux diagnosis using spatial structure in land surface model residuals. *Biogeosciences*, *10*, 4607–4625. http://doi.org/10.5194/bg-10-4607-2013

Hong, S. Y., Noh, Y., & Dudhia, J. (2006). A new vertical diffusion package with an explicit treatment of entrainment processes. *Monthly Weather Review*, *134*(9), 2318–2341. https://doi.org/10.1175/Mwr3199.1

Hu, X.-M. (2008). Incorporation of the Model of Aerosol Dynamics, Reaction, Ionization, and Dissolution (MADRID) into the Weather Research and Forecasting Model with Chemistry (WRF/Chem): Model development and retrospective applications. (PhD thesis), NC State Univ. Retrieved from http://repository.lib.ncsu.edu/ir/handle/1840.16/5241

Hu, X.-M., Crowell, S. Wang, Q., Zhang, Y., Xue, M., Xiao, X., et al. (2019a). CO_2 dynamical downscaling in 2016 over the contiguous United States using WRF-VPRM, a weather-biosphere-online-coupled model. The 99th AMS Annual Meeting, 7 Jan. 2019, Phoenix, AZ

Hu, X.-M., Crowell, S., Wang, Q., Zhang, Y., Davis, K. J., Xue, M., Xiao, X., Moore, B., Wu, X., Choi, Y., & DiGangi, J. P. (2020). Dynamical Downscaling of CO_2 in 2016 over the contiguous United States using WRF-VPRM, a weather-biosphere-online-coupled model. *Journal of Advances in Modeling Earth System*. http://doi.org/10.1029/2019MS001875

Hu, X.-M., Klein, P. M., & Xue, M. (2013). Evaluation of the updated YSU planetary boundary layer scheme within WRF for wind resource and air quality assessments. *Journal of Geophysical Research*, *118*(18), 10,490–10,505. http://doi.org/10.1002/jgrd.50823

Hu, X.-M., Ma, Z., Lin, W., Zhang, H., Hu, J., Wang, Y., et al. (2014). Impact of the loess plateau on the atmospheric boundary layer structure and air quality in the North China Plain: A case study. *Science of the Total Environment*, *499*, 228–237. http://doi.org/10.1016/j.scitotenv.2014.08.053

Hu, X.-M., Nielsen-Gammon, J. W., & Zhang, F. (2010a). Evaluation of three planetary boundary layer schemes in the WRF model. *Journal of Applied Meteorology and Climatology*, *49*, 1831–1844. http://doi.org/10.1175/2010JAMC2432.1

Hu, X.-M., Xue, M., Kong, F., & Zhang, H. (2019b). Meteorological conditions during an ozone episode in Dallas-Fort Worth, Texas and impact of their modeling uncertainties on air quality prediction. *Journal of Geophysical Research-Atmospheres*, *124*(4), 1941–1961. http://doi.org/10.1029/2018JD029791

Hu, X.-M., Xue, M., & McPherson, R. A. (2017). The importance of soil-type contrast in modulating August precipitation distribution near the Edwards Plateau and Balcones Escarpment in Texas. *Journal of Geophysical Research*, *122*(20), 10,711–10,728. http://doi.org/10.1002/2017JD027035

Hu, X.-M., Xue, M., McPherson, R. A., Martin, E., Rosendahl, D. H., & Qiao, L. (2018). Precipitation dynamical downscaling over the Great Plains. *Journal of Advances in Modeling Earth Systems*, *10*(2), 421–447. http://doi.org/10.1002/2017ms001154

Hu, X. M., Zhang, F., & Nielsen-Gammon, J. W. (2010b). Ensemble-based simultaneous state and parameter estimation for treatment of mesoscale model error: A real-data study. *Geophysical Research Letters*, *37*(8). https://doi.org/10.1029/2010GL043017

Huang, W. (2019). Forest condition change, tenure reform, and government-funded eco-environmental programs in Northeast China. *Forest Policy and Economics*, *98*, 67–74. http://doi.org/10.1016/j.forpol.2018.09.003

Huete, A., Didan, K., Miura, T., Rodriguez, E. P., Gao, X., & Ferreira, L. G. (2002). Overview of the radiometric and biophysical performance of the MODIS vegetation indices. *Remote Sensing of Environment*, *83*(1–2), 195–213. http://doi.org/10.1016/S0034-4257(02)00096-2

Hurwitz, M. D., Ricciuto, D. M., Bakwin, P. S., Davis, K. J., Wang, W. G., Yi, C. X., & Butler, M. P. (2004). Transport of carbon dioxide in the presence of storm systems over a Northern Wisconsin forest. *Journal of the Atmospheric Sciences*, *61*(5), 607–618. http://doi.org/10.1175/1520-0469(2004)061<0607:Tocdit>2.0.Co;2

Jamroensan, A. (2013). Improving bottom-up and top-down estimates of carbon fluxes in the Midwestern USA, PhD (Doctor of Philosophy) thesis, University of lowa, http://doi.org/10.17077/etd.99sd8cdc

Jia, Q., Wang, X., Bin, Y., & Wen, R. (2018). Research on the construction of ecological and agrometeorological filed experimental base in Northeast China. *Journal of Meteorological Research*, *34*(6), 161–168. (in Chinese)

Jia, Q., Yu, W., Zhou, L., & Liang, C. (2017). Atmospheric and surface-condition effects on CO_2 exchange in the Liaohe Delta Wetland, China. *Watermark*, *9*(10), 806. http://doi.org/10.3390/w9100806

Jiang, F., Chen, J. M., Zhou, L., Ju, W., Zhang, H., Machida, T., et al. (2016). A comprehensive estimate of recent carbon sinks in China using both top-down and bottom-up approaches. *Scientific Reports*, *6*(1), 1–9. http://doi.org/10.1038/srep22130

Kanamitsu, M., Ebisuzaki, W., Woollen, J., Yang, S. K., Hnilo, J. J., Fiorino, M., & Potter, G. L. (2002). NCEP-DOE AMIP-II reanalysis (R-2). *Bulletin of the American Meteorological Society*, *83*(11), 1631–1644. http://doi.org/10.1175/Bams-83-11-1631

Keenan, T. F., Prentice, I. C., Canadell, J. G., Williams, C. A., Wang, H., Raupach, M., & Collatz, G. J. (2016). Recent pause in the growth rate of atmospheric CO_2 due to enhanced terrestrial carbon uptake. *Nature Communications*, *7*(1), 13428. http://doi.org/10.1038/ncomms13428

Kiel, M., O'Dell, C. W., Fisher, B., Eldering, A., Nassar, R., MacDonald, C. G., & Wennberg, P. O. (2019). How bias correction goes wrong: Measurement of X_{CO2} affected by erroneous surface pressure estimates. *Atmospheric Measurement Techniques*, *12*(4), 2241–2259. https://doi.org/10.5194/amt-12-2241-2019

Knorr, W. (2000). Annual and interannual CO_2 exchanges of the terrestrial biosphere: Process-based simulations and uncertainties. *Global Ecology and Biogeography*, *9*(3), 225–252. https://doi.org/10.1046/j.1365-2699.2000.00159.x

Krause, G. H., & Weis, E. (1991). Chlorophyll fluorescence and photosynthesis: The basics. *Annual Review of Plant Physiology and Plant Molecular Biology*, *42*(1), 313–349. http://doi.org/10.1146/annurev.42.060191.001525

Krishnamurti, T. N., Kishtawal, C. M., Zhang, Z., LaRow, T., Bachiochi, D., Williford, E., et al. (2000). Multimodel ensemble forecasts for weather and seasonal climate. *Journal of Climate*, *13*(23), 4196–4216. http://doi.org/10.1175/1520-0442(2000)013<4196:MEFFWA>2.0.CO;2

Kuang, X., Zhang, Y., & Liu, J. (2007). Seasonal variations of the East Asian subtropical westerly jet and the thermal mechanism. *Acta Meterologica Sinica*, *22*(6), 831–840. https://doi.org/10.1007/BF02918683

Le Quéré, C., Moriarty, R., Andrew, R. M., Canadell, J. G., Sitch, S., Korsbakken, J. I., & Zeng, N. (2015). Global Carbon Budget 2015. *Earth System Science Data*, *7*(2), 349–396. http://doi.org/10.5194/essd-7-349-2015

Li, X., Hu, X.-M., Ma, Y., Wang, Y., Li, L., & Zhao, Z. (2019). Impact of planetary boundary layer on the formation and evolution of air-pollution episodes in Shenyang, Northeast China. *Atmospheric Environment*, *214*, 116850. https://doi.org/10.1016/j.atmosenv.2019.116850

Li, X., Jia, Q., & Liu, J. (2016). Seasonal variations in heat and carbon dioxide fluxes observed over a reed wetland in northeast China. *Atmospheric Environment*, *127*, 6–13. http://doi.org/10.1016/j.atmosenv.2015.11.058

Li, X., Jia, Q., Liu, J., Li, R., Xie, Y., & Liu, G. (2018). Annual cycle of heat and CO_2 fluxes over an artificial rice wetland in the Liaohe Delta of China. *Advances in Engineering Research*, *174*, 316–326. http://doi.org/10.2991/edep-18.2018.50

Liang, W., Shi, Y., Zhang, H., Yue, J., & Huang, G. H. (2007). Greenhouse gas emissions from northeast China rice fields in fallow season. *Pedosphere*, *17*(5), 630–638. http://doi.org/10.1016/S1002-0160(07)60075-7

Liu, C., Huang, J. P., Diao, Y. W., Wen, X. F., Xiao, W., Zhang, M., et al. (2015). Optimization and evaluation of Vegetation Photosynthesis and Respiration Model using the measurements collected from the forest site of subtropical coniferous-evergreen. *Chinese Journal of Plant Ecology*, *39*(4), 388–397. (in Chinese)

Liu, Y., Yue, T., Zhang, L., Zhao, N., Zhao, M., & Liu, Y. (2018). Simulation and analysis of XCO_2 in North China based on high accuracy surface modeling. *Environmental Science and Pollution Research*, *25*(27), 27,378–27,392. http://doi.org/10.1007/s11356-018-2683-x

Lloyd, J., & Taylor, J. A. (1994). On the temperature dependence of soil respiration. *Functional Ecology*, *8*(3), 315–323. http://doi.org/10.2307/2389824

Mahadevan, P., Wofsy, S. C., Matross, D. M., Xiao, X., Dunn, A. L., Lin, J. C., et al. (2008). A satellite-based biosphere parameterization for net ecosystem CO_2 exchange: Vegetation Photosynthesis and Respiration Model (VPRM). *Global Biogeochemical Cycles*, *22*(2), GB2005. http://doi.org/10.1029/2006GB002735

Matsushita, B., Yang, W., Chen, J., Onda, Y., & Qiu, G. (2007). Sensitivity of the enhanced vegetation index (EVI) and normalized difference vegetation index (NDVI) to topographic effects: a case study in high-density cypress forest. *Sensors*, *7*(11), 2636–2651. https://doi.org/10.3390/s7112636

Mauder, M., Foken, T., Clement, R., Elbers, J. A., Eugster, W., Grünwald, T., et al. (2008). Quality control of CarboEurope flux data? Part 2: Inter-comparison of eddy-covariance software. *Biogeosciences, European Geosciences Union (EGU)*, *5*(2), 451–462. http://doi.org/10.5194/bg-5-451-2008

Mlawer, E. J., Taubman, S. J., Brown, P. D., Iacono, M. J., & Clough, S. A. (1997). Radiative transfer for inhomogeneous atmospheres: RRTM, a validated correlated-k model for the longwave. *Journal of Geophysical Research*, *102*(D14), 16,663–16,682. https://doi.org/10.1029/97jd00237

Morrison, H., Thompson, G., & Tatarskii, V. (2009). Impact of cloud microphysics on the development of trailing stratiform precipitation in a simulated squall line: comparison of one- and two-moment schemes. *Monthly Weather Review*, *137*(3), 991–1007. http://doi.org/10.1175/2008mwr2556.1

Nielsen-Gammon, J. W., Hu, X.-M., Zhang, F., & Pleim, J. E. (2010). Evaluation of planetary boundary layer scheme sensitivities for the purpose of parameter estimation. *Monthly Weather Review*, *138*(9), 3400–3417. http://doi.org/10.1175/2010MWR3292.1

Olsen, S. C., & Randerson, J. T. (2004). Dierences between surface and column atmospheric CO_2 and implications for carbon cycle research. *Journal of Geophysical Research*, *114*(D18), D02301. https://doi.org/10.1029/2008JD011465

Parazoo, N. C., Denning, A. S., Berry, J. A., Wolf, A., Randall, D. A., Kawa, S. R., et al. (2011). Moist synoptic transport of CO_2 along the mid-latitude storm track. *Geophysical Research Letters*, *38*(9), L09804. http://doi.org/10.1029/2011gl047238

Park, C., Gerbig, C., Newman, S., Ahmadov, R., Feng, S., Gurney, K. R., et al. (2018). CO_2 transport, variability, and budget over the Southern California Air Basin using the high-resolution WRF-VPRM model during the CalNex 2010 campaign. *Journal of Applied Meteorology and Climatology*, *57*(6), 1337–1352. http://doi.org/10.1175/jamc-d-17-0358.1

Peters, W., Jacobson, A. R., Sweeney, C., Andrews, A. E., Conway, T. J., Masarie, K., et al. (2007). An atmospheric perspective on North American carbon dioxide exchange: CarbonTracker. *Proceedings of the National Academy of Sciences*, *104*(48), 18,925–18,930. http://doi.org/10.1073/pnas.0708986104

Peylin, P., Law, R. M., Gurney, K. R., Chevallier, F., Jacobson, A. R., Maki, T., et al. (2013). Global atmospheric carbon budget: Results from an ensemble of atmospheric CO_2 inversions. *Biogeosciences*, *10*(10), 6699–6720. http://doi.org/10.5194/bg-10-6699-2013

Piao, S., Fang, J., Ciais, P., Peylin, P., Huang, Y., Sitch, S., & Wang, T. (2009). The carbon balance of terrestrial ecosystems in China. *Nature*, *458*(7241), 1009–1013. http://doi.org/10.1038/nature07944

Piao, S., Sitch, S., Ciais, P., Friedlingstein, P., Peylin, P., Wang, X., et al. (2013). Evaluation of terrestrial carbon cycle models for their response to climate variability and to CO_2 trends. *Global Change Biology*, *19*(7), 2117–2132. https://doi.org/10.1111/gcb.12187

Pillai, D., Gerbig, C., Ahmadov, R., Rödenbeck, C., Kretschmer, R., Koch, T., et al. (2011). High-resolution simulations of atmospheric CO_2 over complex terrain—Representing the Ochsenkopf mountain tall tower. *Atmospheric Chemistry and Physics*, *11*(15), 7445–7464. http://doi.org/10.5194/acp-11-7445-2011

Pinder, R. W., Gilliam, R. C., Appel, K. W., Napelenok, S., Foley, K. M., & Gilliland, A. B. (2008). Efficient Probabilistic Estimates of Surface Ozone Concentration Using an Ensemble of Model Configurations and Direct Sensitivity Calculations. *Environmental Science & Technology*, *43*(7), 2388–2393. https://doi.org/10.1021/es8025402

Pury, D. D., & Farquhar, G. D. (1997). Simple scaling of photosynthesis from leaves to canopies without the errors of big-leaf models. *Plant, Cell & Environment*, *20*(5), 537–557. https://doi.org/10.1111/j.1365-3040.1997.00094.x

Rayner, P. J., & O'Brien, D. M. (2001). The utility of remotely sensed CO_2 concentration data in surface source inversions. *Geophysical Research Letters*, *28*(1), 175–178. http://doi.org/10.1029/2000GL011912

Rayner, P. J., Utembe, S. R., & Crowell, S. (2014). Constraining regional greenhouse gas emissions using geostationary concentration measurements: a theoretical study. *Atmospheric Measurement Techniques*, *7*(10), 3285–3293. http://doi.org/10.5194/amt-7-3285-2014

Ren, X., Wang, Q., Tong, C., Wu, J., Wang, K., Zhu, Y., et al. (2007). Estimation of soil respiration in a paddy ecosystem in the subtropical region of China. *Chinese Science Bulletin*, *52*(19), 2722–2730. http://doi.org/10.1007/s11434-007-0346-2

Reuter, M., Buchwitz, M., Hilker, M., Heymann, J., Bovensmann, H., Burrows, J. P., et al. (2017). How much CO_2 is taken up by the European terrestrial biosphere? *Bulletin of the American Meteorological Society*, *98*(4), 665–671. http://doi.org/10.1175/BAMS-D-15-00310.1

Rind, D., Suozzo, R., Balachandran, N. K., & Prather, M. J. (1990). Climate change and the middle atmosphere. Part I: The doubled CO_2 climate. *Journal of the Atmospheric Sciences*, *47*(4), 475–494. http://doi.org/10.1175/1520-0469(1990)047<0475:CCATMA>2.0.CO;2

Running, S. W., Nemani, R. R., Heinsch, F. A., Zhao, M., Reeves, M., & Hashimoto, H. (2004). A continuous satellite-derived measure of global terrestrial primary production. *Bioscience*, *54*(6), 547–560. https://doi.org/10.1641/0006-3568(2004)054[0547:ACSMOG]2.0.CO;2

Schimel, D., Stephens, B. B., & Fisher, J. B. (2015). Effect of increasing CO_2 on the terrestrial carbon cycle. *Proceedings of the National Academy of Sciences*, *112*(2), 436–441. http://doi.org/10.1073/pnas.1407302112

Seo, J., Kang, S. M., & Merlis, T. M. (2017). A model intercomparison of the tropical precipitation response to a CO_2 doubling in aquaplanet simulations. *Geophysical Research Letters*, *44*(2), 993–1000. https://doi.org/10.1002/2016GL072347

Shi, H., Li, L., Eamus, D., Huete, A., Cleverly, J., Tian, X., et al. (2017). Assessing the ability of MODIS EVI to estimate terrestrial ecosys-temgross primary production of multiple land cover types. *Ecological Indicators*, *72*, 153–164. https://doi.org/10.1016/j.ecolind.2016.08.022

Shi, Z., Crowell, S. M. R., Luo, Y., & Moore, B. III (2018). Model structures amplify uncertainty in predicted soil carbon responses to climate change. *Nature Communications*, *9*(1), 2171. https://doi.org/10.1038/s41467-018-04526-9

Singh, H. A., Rasch, P. J., & Rose, B. E. J. (2017). Increased ocean heat convergence into the high latitudes with CO_2 doubling enhances polar-amplified warming. *Geophysical Research Letters*, *44*(20), 10,583–10,591. https://doi.org/10.1002/2017GL074561

Song, T., Wang, Y., Song, C., Shi, L., Huang, Y., & Wang, P. (2006). CO_2 fluxes from rice fields of Sanjiang plain and its environmental response factors. *China Environmental Science*, *26*(6), 657–661. (in Chinese)

Sun, Y., Frankenberg, C., Jung, M., Joiner, J., Guanter, L., Köhler, P., & Magney, T. (2018). Overview of Solar-Induced chlorophyll Fluorescence (SIF) from the Orbiting Carbon Observatory-2: Retrieval, cross-mission comparison, and global monitoring for GPP. *Remote Sensing of Environment*, *209*, 808–823. http://doi.org/10.1016/j.rse.2018.02.016

Szulejko, J. E., Kumar, P., Deep, A., & Kim, K. H. (2017). Global warming projections to 2100 using simple CO_2 greenhouse gas modeling and comments on CO_2 climate sensitivity factor. *Atmospheric Pollution Research*, *8*(1), 136–140. https://doi.org/10.1016/j.apr.2016.08.002

Takahashi, T., Sutherland, S. C., Wanninkhof, R., Sweeney, C., Feely, R. A., Chipman, D. W., et al. (2009). Climatological mean and decadal change in surface ocean pCO_2, and net sea-air CO_2 flux over the global oceans. *Deep-Sea Research Part II: Topical Studies in Oceanography*, *56*(8–10), 554–577. http://doi.org/10.1016/j.dsr2.2008.12.009

Tang, J., Bolstad, P. V., Desai, A. R., Martin, J. G., Cook, B. D., Davis, K. J., & Carey, E. V. (2008). Ecosystem respiration and its components in an old-growth forest in the Great Lakes region of the United States. *Agricultural and Forest Meteorology*, *148*(2), 171–185. http://doi.org/10.1016/j.agrformet.2007.08.008

Thomas, A., Huff, A., Hu, X.-M., & Zhang, F. (2019). Quantifying uncertainties of ground-level ozone within WRF-Chem simulations in the Mid-Atlantic Region of the United States as a response to variability. *Journal of Advances in Modeling Earth Systems*, *11*(4), 1100–1116. https://doi.org/10.1029/2018MS001457

Thompson, R. L., Patra, P. K., Chevallier, F., Maksyutov, S., Law, R. M., & Ziehn, et al. (2016). Top–down assessment of the Asian carbon budget since the mid 1990s. *Nature Communications*, *7*(1), 10724. https://doi.org/10.1038/ncomms10724

Tian, H., Xu, X., Lu, C., Liu, M., Ren, W., Chen, G., et al. (2011). Net exchanges of CO_2, CH_4, and N_2O between China's terrestrial ecosystems and the atmosphere and their contributions to global climate warming. *Journal of Geophysical Research – Biogeosciences*, *116*, G02011. http://doi.org/10.1029/2010JG0013

Turner, D. P., Ritts, W. D., Styles, J. M., Yang, Z., Cohen, W. B., Law, B. E., & Thornton, P. E. (2006). A diagnostic carbon flux model to monitor the effects of disturbance and interannual variation in climate on regional NEP. *Tellus B*, *58*(5), 476–490. http://doi.org/10.1111/j.1600-0889.2006.00221.x

Uccellini, L. W., & Johnson, D. R. (1979). The coupling of upper and lower tropospheric jet streaks and implications for the development of severe convective storms. *Monthly Weather Review*, *107*(6), 682–703. https://doi.org/10.1175/1520-0493(1979)107<0682:TCOUAL>2.0.CO;2

Veroustraete, F., Sabbe, H., & Eerens, H. (2002). Estimation of carbon mass fluxes over Europe using the C-Fix model and Euroflux data. *Remote Sensing of Environment*, *83*(3), 376–399. http://doi.org/10.1016/S0034-4257(02)00043-3

Wang, H. M., Saigusa, N., Zu, Y. G., Wang, W. J., Yamamoto, S., & Kondo, H. (2008). Carbon fluxes and their response to environmental variables in a Dahurian larch forest ecosystem in northeast China. *Journal of Forestry Research*, *19*(1), 1–10. http://doi.org/10.1007/s11676-008-0001-z

Wang, J. L., & Kotamarthi, V. R. (2014). Downscaling with a nested regional climate model in near-surface fields over the contiguous United States. *Journal of Geophysical Research*, *119*(14), 8778–8797. https://doi.org/10.1002/2014jd021696

Wexler, H. (1961). A boundary layer interpretation of the low-level jet. *Tellus*, *13*(3), 368–378. https://doi.org/10.1111/j.2153-3490.1961.tb00098.x

White, M. A., Thornton, P. E., Running, S. W., & Nemani, R. R. (2000). Parameterization and sensitivity analysis of the BIOME-BGC terrestrial ecosystem model: Net primary production controls. *Earth Interactions*, *4*(3), 1–85. https://doi.org/10.1175/1087-3562(2000)004<0003:PASAOT>2.0.CO;2

WMO Greenhouse Gas Bulletin (2017). *The state of greenhouse gases in the atmosphere based on global observations through 2016*. Geneva: World Meteorological Organization.

Wu, H., Sun, T., Fan, Z., & Zhao, L. (2014). The major food crops in response to climate change and its yield effect in Northeast of China. *Journal of Agricultural Resources and Environment*, *31*(4), 299–307. (in Chinese)

Xiao, J., Zhuang, Q., Baldocchi, D. D., Law, B. E., Richardson, A. D., Chen, J., et al. (2008). Estimation of net ecosystem carbon exchange for the conterminous United States by combining MODIS and AmeriFlux data. *Agricultural and Forest Meteorology*, *148*(11), 1827–1847. https://doi.org/10.1016/j.agrformet.2008.06.015

Xiao, X. M., Zhang, Q. Y., Braswell, B., Urbanski, S., Boles, S., Wofsy, S., et al. (2004). Modeling gross primary production of temperate deciduous broadleaf forest using satellite images and climate data. *Remote Sensing of Environment*, *91*(2), 256–270. https://doi.org/10.1016/j.rse.2004.03.010

Xie, Y., Lin, H., Ye, Y., & Ren, X. (2019). Changes in soil erosion in cropland in northeastern China over the past 300 years. *Catena*, *176*, 410–418. http://doi.org/10.1016/j.catena.2019.01.026

Xu, Y., Ke, C., Zhan, W., Li, H., & Yao, L. (2017). Variations in satellite-derived carbon dioxide over different regions of China from 2003 to 2011. *Atmospheric Environment*, *150*, 379–388. https://doi.org/10.1016/j.atmosenv.2016.11.032

Yang, D., Liu, Y., Cai, Z., & Deng, J. (2016). The spatial and temporal distribution of carbon dioxide over China based on GOSAT observations. *Chinese Journal of Atmospheric Sciences*, *40*(3), 541–550. http://doi.org/10.3878/j.issn.1006-9895.1508.14121 (in Chinese)

Yang, D. X., Liu, Y., Cai, Z. N., Chen, X., Yao, L., & Lu, D. R. (2018). First global carbon dioxide maps produced from TanSat measurements. *Advances in Atmospheric Sciences*, *35*(6), 621–623. https://doi.org/10.1007/s00376-018-7312-6

Yang, J., Liu, J., Hu, X., Li, X., Wang, Y., & Li, H. (2013). Effect of water table level on CO_2, CH_4 and N_2O emissions in a freshwater marsh of Northeast China. *Soil Biology and Biochemistry*, *61*, 52–60. http://doi.org/10.1016/j.soilbio.2013.02.009

Ye, X., Lauvaux, T., Kort, E. A., Oda, T., Feng, S., Lin, J. C., et al. (2017). Constraining fossil fuel CO_2 emissions from urban area using OCO-2 observations of total column CO_2. *Atmospheric Chemistry and Physics Discussions*, 1–30. http://doi.org/org/10.5194/acp-2017-1022

Yuan, W., Liu, S., Cai, W., Dong, W., Chen, J., Arain, A., et al. (2013). Are vegetation-specific model parameters required for estimating gross primary production? *Geoscientific Model Development Discussion*, *6*(4), 5475–5488. http://doi.org/10.5194/gmdd-6-5475-2013

Yuan, W., Liu, S., Zhou, G., Zhou, G., Tieszen, L. L., Baldocchi, D., et al. (2007). Deriving a light use efficiency model from eddy covariance flux data for predicting daily gross primary production across biomes. *Agricultural and Forest Meteorology*, *143*(3–4), 189–207. http://doi.org/10.1016/j.agrformet.2006.12.001

Yuan, W. P., Cai, W. W., Xia, J. Z., Chen, J., Liu, S., Dong, W., et al. (2014). Global comparison of light use efficiency models for simulating terrestrial vegetation gross primary production based on the LaThuile database. *Agricultural and Forest Meteorology*, *192-193*, 108–120. http://doi.org/10.1016/j.agrformet.2014.03.007

10.1029/2019JD031686

Yuan, Y., Sussmann, R., Rettinger, M., Ries, L., Petermeier, H., & Menzel, A. (2019). Comparison of continuous in-situ CO_2 measurements with co-located column-averaged XCO_2 TCCON/Satellite observations and CarbonTracker model over the Zugspitze region. *Remote Sensing*, *11*(24), 2981. https://doi.org/10.3390/rs11242981

Yue, C., Ciais, P., Bastos, A., Chevallier, F., Yin, Y., Rödenbeck, C., & Park, T. (2017). Vegetation greenness and land carbon-flux anomalies associated with climate variations: a focus on the year 2015. *Atmospheric Chemistry and Physics*, *17*(22), 13,903–13,919. https://doi.org/10.5194/acp-17-13903-2017

Zhang, F., Bei, N., Nielsen-Gammon, J. W., Li, G., Zhang, R., Stuart, A., & Aksoy, A. (2007). Impacts of meteorological uncertainties on ozone pollution predictability estimated through meteorological and photochemical ensemble forecasts. *Journal of Geophysical Research-Atmospheres*, *112*(D4), D04304. https://doi.org/10.1029/2006JD007429

Zhang, H. F., Chen, B. Z., van der Laan-Luijkx, I. T., Chen, J., Xu, G., Yan, J. W., et al. (2014). Net terrestrial CO_2 exchange over China during 2001–2010 estimated with an ensemble data assimilation system for atmospheric CO_2. *Journal of Geophysical Research-Atmospheres*, *119*(6), 3500–3515. http://doi.org/10.1002/2013JD021297

Zhang, J. B., Song, C. C., & Yang, W. Y. (2005). Cold season CH_4, CO_2 and N_2O fluxes from freshwater marshes in northeast China. *Chemosphere*, *59*(11), 1703–1705. http://doi.org/10.1016/j.chemosphere.2004.11.051

Zhang, J. R., Wang, Y. W., Zhang, M., Diao, Y. W., & Liu, C. (2017a). Opitimization and validation of the Vegetation Photosynthesis and Respiration Model in a temperate broad-leaved Korean pine forest. *Acta Ecologica Sinica*, *37*(20), 6679–6690. http://doi.org/10.5846/stxb201607291552 (in Chinese)

Zhang, Y., Xiao, X., Wu, X., Zhou, S., Zhang, G., Qin, Y., & Dong, J. (2017b). A global moderate resolution dataset of gross primary production of vegetation for 2000–2016. *Scientific Data*, *4*(1), 170165. http://doi.org/10.1038/sdata.2017.165

Zhang, Y., Zhang, F., Stensrud, D. J., & Meng, Z. (2016). Intrinsic predictability of the 20 May 2013 tornadic thunderstorm event in Oklahoma at storm scales. *Monthly Weather Review*, *144*(4), 1273–1298. https://doi.org/10.1175/MWR-D-15-0105.1

Zhong, S., Fast, J. D., & Bian, X. (1996). A case study of the Great Plains low-level jet using wind profiler network data and a high-resolution mesoscale model. *Monthly Weather Review*, *124*(5), 785–806. https://doi.org/10.1175/1520-0493(1996)124<0785:ACSOTG>2.0.CO;2

Zhou, L., Zhou, G., & Jia, Q. (2009). Annual cycle of CO_2 exchange over a reed (Phragmites australis) wetland in Northeast China. *Aquatic Botany*, *91*(2), 91–98. http://doi.org/10.1016/j.aquabot.2009.03.002

Zhou, Y., Xiao, X., Zhang, G., Wagle, P., Bajgain, R., Dong, J., et al. (2017). Quantifying agricultural drought in tallgrass prairie region in the U.S. Southern Great Plains through analysis of a water-related vegetation index from MODIS images. *Agricultural and Forest Meteorology*, *246*, 111–122. http://doi.org/10.1016/j.agrformet.2017.06.007

Zhu, W. Q., Chen, Y. H., Xu, D., & Li, J. (2005). Advances in terrestrial net primary productivity (NPP) estimation models. *Chinese Journal of Ecology*, *24*, 296–300. (in Chinese)

Zhu, Z. L., Sun, X. M., Wen, X. F., Zhou, Y. L., Tian, J., & Yuan, G. F. (2006). Study on the processing method of nighttime CO_2 eddy covariance flux data in China FLUX. *Science in China Series D: Earth Sciences*, *49*(S2), 36–46. http://doi.org/10.1007/s11430-006-8036-5